Master's thesis

NTNU
Norwegian University of Science and Technology
Faculty of Natural Sciences
Department of Physics

Sebastian Albert Dahl Sandbu

# Segmentation of the Cervical Spine based on 7T MRI

Master's thesis in Applied Physics and Mathematics
Supervisor: Johanna Vannesjö
Co-supervisor: Maria Tunset Grinde
July 2023

NTNU
Norwegian University of
Science and Technology

Sebastian Albert Dahl Sandbu

# Segmentation of the Cervical Spine based on 7T MRI

Master's thesis in Applied Physics and Mathematics
Supervisor: Johanna Vannesjö
Co-supervisor: Maria Tunset Grinde
July 2023

Norwegian University of Science and Technology
Faculty of Natural Sciences
Department of Physics

NTNU
Norwegian University of
Science and Technology

NTNU
Kunnskap for en bedre verden

Department of Physics

TFY4910 - Biophysics, Master Thesis

# Segmentation of the Cervical Spine based on 7T MRI

*Author:*
Sebastian A D Sandbu

24.07.2023

# Preface

This master thesis was performed in the spring semester of 2023 at the Department of Physics at the Norwegian University of Science and Technology (NTNU).

In this master thesis, a method for simulating induced magnetic field distortions in the spinal canal from a segmentation of the cervical spine was tested. A pre-project report was written during the fall of 2022, [1], which created the basis for the work performed in this master thesis. The method used was initially validated in the project report, where it was tested on a 3D printed model of the middle part of the cervical spine (C3-C5), acquired from a CT database.

The past months have been both hectic and instructive. Hardware problems caused delay in the scanning of the volunteers, and time went by. These problems were eventually solved, and I could begin solving the task at hand. A great amount of time was invested in searching for and testing software for segmentation of MRI. In the end, I opted for ITK-SNAP as my segmentation software because of its main domain as a segmentation tool, and also because of its simplicity and range of segmentation methods. A lot of time has also been invested in Matlab, a program I am beginning to grasp.

I would like to thank my supervisor prof. Johanna Vannesjö for trusting me with this project. This semester she has had maternal leave, and her in depth knowledge has been greatly missed. I would also thank my co-supervisor Maria Tunset Grinde for stepping in, and for assisting and counseling me throughout this semester. Prof. Ruth Catharina de Lange Davies at the Institute of Physics has provided me with additional feedback, which I highly appreciate. Although the master thesis is independent work, their knowledge and feedback has been invaluable. Finally, I would like to thank the volunteers for taking their time to be part of my thesis.

# Abstract

Ultra high field (UHF) MRI, such as 7T, has the potential to improve image quality of MRI through better signal-to-noise ratio (SNR) and increased resolution. However, UHF MRI also introduces more pronounced susceptibility artifacts from the increased $B_0$ field strength.
Magnetic susceptibility, denoted as $\chi$, is a measure of a material's tendency to be magnetized when exposed to a magnetic field, and its distribution throughout the body induces inhomogeneities in the main magnetic field, resulting in artifacts such as signal loss and geometric distortions. This is especially a concern in the neck region, which consists of rapidly changing susceptibility values from the cervical vertebrae and soft tissue in between the vertebrae. Our current shimming techniques are not able to correct these field distortions. The ability to attain patient specific $B_0$ field maps can offer valuable insight to enhance patient specific shimming techniques.
The work performed in this thesis can improve image quality of MRI of the spinal cord, and thus improving diagnosis of diseases and conditions involving the spinal cord.

In this master thesis, segmentations of the cervical spine from 7T MR images of five healthy volunteers were utilized to compute the induced magnetic field from the susceptibility distribution in the cervical spine. The first part of the thesis involved selection of a suitable software to extract the cervical spine from the MRI data. A comprehensive review article studying segmentation software of MRI was used as a guideline for choosing the segmentation software. The article ranked the segmentation software ITK-SNAP as the overall best choice for MRI segmentation. ITK-SNAP was used in this thesis to obtain manual, semi-automatic and automatic segmentations. A quantitative analysis was conducted to evaluate the automatic segmentation methods, using the manual segmentation as the gold standard. In the second part, a Fourier-based method was employed to quickly calculate magnetic field distortions based on susceptibility maps generated through the manual segmentation of the MR images. The accuracy of the model was evaluated by comparing the simulated field maps with the field maps measured from the 7T MR system. Additionally, a quantitative analysis of the numerical values from both field maps was conducted.

The automatic segmentation methods are partly successful in segmenting areas with sufficient contrast, particularly the vertebral bodies. In the anterior part of the cervical spine, both methods show difficulties in distinguishing soft tissue from the cervical spine, resulting in segmentation of unwanted areas. The signal in these areas is weaker than the signal in the posterior part of the cervical spine, due to the use of a surface coil. Increased contrast in these regions should improve the automatic segmentation methods. Simulation of the induced magnetic field from a uniform susceptibility distribution in the cervical spine were performed for four subjects. The simulated field maps and the measured field show remarkable resemblance. The linear regression analysis between the simulated and measured field maps show similar trends, and was used to calculate the mean of the susceptibility difference between bone and soft tissue to be approximately -1.28 ppm.

The work in this master's thesis can contribute to increased knowledge about segmentation of bones from MRI, and how the susceptibility distribution in the cervical spine creates distortions in the $B_0$ magnetic field, affecting image quality in MRI of the spinal cord. The ultimate goal is to improve patient-specific shimming techniques based on direct segmentation from the MRI scanner, which have the potential to enhance image quality and accuracy in future studies of the spinal cord using 7T MRI.

# Sammendrag

Ultrahøyfelt-MR (UHF-MR), som 7T, har potensial til å forbedre bildekvaliteten i MR-undersøkelser gjennom økt oppløsning og forbedret signal-til-støy-forhold (SNR). Imidlertid introduserer UHF-MR også mer markante susceptibilitetsartefakter på grunn av økt magnetfeltstyrke. Magnetisk susceptibilitet, betegnet som $\chi$, er en måling av et materials tendens til å bli magnetisert når det utsettes for et magnetisk felt, og dets fordeling gjennom kroppen forårsaker ujevnheter i det primære magnetiske feltet, noe som resulterer i artefakter som signaltap og geometriske forvrengninger. Dette er spesielt en bekymring i nakkeområdet, som består av raskt skiftende susceptibilitetsverdier fra nakkevirvler og mykt vev mellom virvlene. Våre nåværende shimming-teknikker er ikke i stand til å korrigere disse feltforvrengningingene. Evnen til å oppnå pasientspesifikke $B_0$-feltkart kan gi verdifull innsikt for å forbedre pasientspesifikke shimming-teknikker. Et fremtidig mål for forskningen utført i denne masterstudien er å forbedre bildekvaliteten i MRI av ryggmargen og dermed forbedre diagnosen av sykdom og skader i ryggmargen.

I denne masteroppgaven ble segmenteringer av nakkevirvlene fra 7T-MR på friske frivillige brukt til å beregne det induserte magnetiske feltet basert på susceptibilitetsfordelingen i nakkevirvlene. Den første delen av oppgaven innebar valg av egnet programvare for å segmentere nakkevirvlene fra MR-bildene. Et litteraturstudie som undersøkte segmenteringsprogramvarer for MRI ble brukt som retningslinje for valg av segmenteringsprogramvare. Artikkelen rangerte segmenteringsprogramvaren ITK-SNAP som det beste valget for MR-segmentering. ITK-SNAP ble brukt i denne oppgaven for å oppnå og sammenligne manuelle, halvautomatiske og automatiske segmenteringer. En kvantitativ analyse ble utført for å evaluere de automatiske segmenteringsmetodene i forhold til den manuelle segmenteringen. I den andre delen ble en Fourier-basert metode benyttet for raskt å beregne magnetiske feltforvrengninger basert på susceptibilitetskart generert gjennom manuell segmentering av MR-bildene. Modellens nøyaktighet ble vurdert ved å sammenligne de simulerte feltkartene med feltkartene generert av skanneren. I tillegg ble det utført en kvantitativ analyse av numeriske verdier fra begge feltkartene.

Den manuelle segmenteringen blir brukt som referanse for å sammenligne de raskere halvautomatiske og automatiske segmenteringsmetodene. De automatiske metodene er delvis vellykkede i å segmentere områder med tilstrekkelig kontrast, spesielt virvelkroppene. I den fremre delen av nakkevirvlene har begge metodene vanskeligheter med å skille mykt vev fra nakkevirvlene, noe som resulterer i segmentering av uønskede områder. Signalet i disse områdene er svakere enn signalet i den bakre delen av nakkevirvlene siden MR opptaket er gjort med en overflatespole. Økt kontrast i disse regionene bør forbedre de automatiske segmenteringsmetodene. Simuleringer av det induserte magnetfeltet fra en uniform susceptibilitetsfordeling i nakkevirvlene ble utført på fire deltakere. De simulerte feltkartene og de målte feltkartene viser en bemerkelsesverdig likhet. Lineær regresjonsanalyse mellom de simulerte og målte feltkartene viser lignende trender og ble brukt til å beregne gjennomsnittet av susceptibilitetsforskjellen mellom bein og bløtvev til å være omtrent -1,28 ppm.

Arbeidet i denne masteroppgaven kan bidra til økt kunnskap om segmentering av bein fra MR-bilder og hvordan susceptibilitetsfordeling i nakkevirvlene skaper forvrengninger i det magnetiske $B_0$-feltet, noe som påvirker bildekvaliteten i MR-bilder av ryggmargen. Det endelige målet er å forbedre pasientspesifikke shimming-teknikker basert på direkte segmentering fra MR-skanneren, noe som har potensiale til å forbedre bildekvaliteten og nøyaktigheten i fremtidige studier av ryggmargen ved bruk av 7T MRI.

# Table of Contents

# List of Figures

# List of Tables

# 1 Introduction

Use of ultra high field (UHF) strengths in MRI, such as 7T, gives considerable increase in the signal-to-noise ratio (SNR). This translates to better spatial resolution or faster exam times. As ultra-high field MRI has become more clinically available, research on spinal cord MRI has been extensively more studied the last couple of years. There are several challenges concerning MRI at 7T, most notably inhomogeneities in the $B_1$ and $B_0$ fields, and increased radio-frequency energy deposition, resulting in higher specific absorption rate (SAR). The work performed in this thesis, is aiming at mitigating $B_0$ inhomogeneities caused by patient-specific susceptibility distributions. This is done by calculating the patient-specific $B_0$ inhomogeneity map from a segmentation of the cervical spine. The computed field may be used to improve patient-specific shimming in UHF MRI of the cervical spinal cord.

Magnetic resonance imaging (MRI) is non-invasive medical imaging technique providing 3D anatomical visualisation of the body. MRI has superior soft tissue contrast compared to other imaging modalities, without the use of ionizing radiation. In MRI, the signal producing the image originates from the spin, or magnetic moment, of the hydrogen protons in the body. Strong magnetic fields align the spins in the body, producing a net magnetization vector. Pulses of magnetic fields in the radio-frequency spectrum excite the spins, and flip the magnetization vector perpendicular to the direction of the main magnetic field. The signal is spatially encoded by employing a time varying gradient magnetic field in each orthogonal direction. In order to obtain optimal image acquisition, MRI require a uniform main magnetic field, $B_0$, and linear gradients, $G_{x,y,z}$. Inhomogeneities in the magnetic field and non-linear gradients causes image artefacts in the form of signal loss and geometric distortions. A main source of inhomogeneities in the $B_0$ field is the susceptibility distribution in the patient.

Magnetic susceptibility, $\chi$, is a measure of the tissue's tendency to be magnetized when placed in a magnetic field. Different tissue are comprised of different molecular compositions, and will therefore have different magnetic susceptibility. Magnetic susceptibility is characterized into three categories: diamagnetic, paramagnetic and super-paramagnetic/ferromagnetic. Diamagnetic tissue have negative value of susceptibility, meaning that they will induce a magnetic field opposing the applied magnetic field. Paramagnetic and ferromagnetic materials have a positive magnetic susceptibility value, and these materials will augment the applied field. Ferromagnetic materials are therefore strictly forbidden in the vicinity of the MR scanner. When a patient is placed in the MR scanner, their specific susceptibility distribution will distort the main magnetic field in a particular way.

Active shimming is the process of correcting the patient-specific $B_0$ inhomogeneities. Today's shimming techniques are not able to fully compensate for the patient-specific $B_0$ inhomogeneities, which is especially problematic in imaging of the spinal cord at higher field strengths. If successful, MRI of the spinal cord would provide enhanced image quality and improved diagnosis of spinal cord injury and disease.

Segmentation of medical images are one of the most important tasks for image analysis. A large part of the segmentation software are developed for CT images or MRI of the brain, ([2]). The intensity values in CT, the Hounsfield unit, are roughly proportional to the density of the tissue. This relationship makes segmentation of CT images a much easier task than segmentation of MRI. A major part of this thesis has been to evaluate software tools for automatic or semi-automatic segmentation of the cervical spine on MRI. The review article titled *Comprehensive Review of 3D Segmentation Software Tools for MRI Usable for Pelvic Surgery Planning*, [2], was used as a

guideline for choosing segmentation software.

The ability to rapidly calculate a patient-specific $B_0$ field map from the susceptibility distribution in the imaging volume have the potential to improve $B_0$ shimming techniques. Segmentation of the cervical spine from 7T MRI are utilized as a model to calculate the induced magnetic field from the susceptibility distribution in the cervical spine. A Fourier-based method described extensively in previous publications, [3, 4], are used to rapidly calculate the patient-specific $B_0$ field maps.

# 2 Theory

The theory section of this master thesis draws on the project assignment conducted in the autumn of 2022, [1]. The entire section has undergone a thorough review, resulting in necessary revisions and the addition of new sections. Furthermore, in the subsection dedicated to basic MRI concepts, the primary reference texts for this subsection include *MRI: Physical Principles and Sequence Design* [5], *Principles of Magnetic Resonance Imaging: A Signal processing Perspective* [6] and *Ultra-high field MRI* [7].

## 2.1 The Basics of MRI

Magnetic resonance imaging (MRI) is a non-invasive medical imaging technique that generates three-dimensional anatomical data visualized in two dimensions. Unlike other imaging modalities, MRI does not employ ionizing radiation and offers high soft-tissue contrast. A distinguishing feature of MRI is its ability to obtain a wide range of contrasts by manipulating the acquisition parameters. This versatility sets MRI apart from other imaging techniques.

### 2.1.1 Nuclear Magnetic Resonance (NMR)

The nucleus of an atom consists of protons and neutrons, collectively known as nucleons. The magnetic properties of the nucleus are determined by the combined spin and charge properties of these individual nucleons.

Spin is a quantum mechanical property associated with subatomic particles, such as electrons, protons, and neutrons. It represents a type of angular momentum inherent to these particles, independent of their motion or external factors. Although similar to the angular momentum of a spinning top, spin is not a physical rotation but an abstract concept described by mathematical equations in quantum mechanics. Unlike classical angular momentum, spin takes only quantized values, limited to a discrete set of possibilities. Particles like electrons, protons, and neutrons have a spin value of 1/2.

Magnetic Resonance Imaging (MRI) is based on the phenomenon of nuclear magnetic resonance (NMR), where nuclei with non-zero spin can absorb and emit electromagnetic radiation at a specific frequency when exposed to a magnetic field. The frequency at which the nuclei absorb energy is known as the Larmor frequency or the natural frequency. While all particles with spin can undergo NMR, hydrogen nuclei $^1H$, that is protons, are often manipulated in MRI due to their strong magnetic properties and abundance in the human body, primarily in the form of water.

To understand the behavior of spins in a magnetic field, the Zeeman effect is observed. This effect describes the splitting of energy levels in particles with spin when subjected to a magnetic field, visualized in Figure 1. In the absence of a magnetic field, the spins are randomly oriented since all directions have equal energy. However, in the presence of a strong magnetic field, the spin states no longer have the same energy. Consequently, the spins align in two possible states: spin up and spin down, corresponding to different energy levels (as illustrated in Figure 2). The energy difference between these states is given by Equation (1):

$$\Delta E = hf = h\gamma B_0, \tag{1}$$

Here, $h$ represents Planck's constant, $\gamma$ is the gyromagnetic ratio, and $B_0$ denotes the applied magnetic field strength. Figure 1 depicts the relationship described by this equation, namely that an increase in the strength of the magnetic field results in a higher energy difference between the spin states.

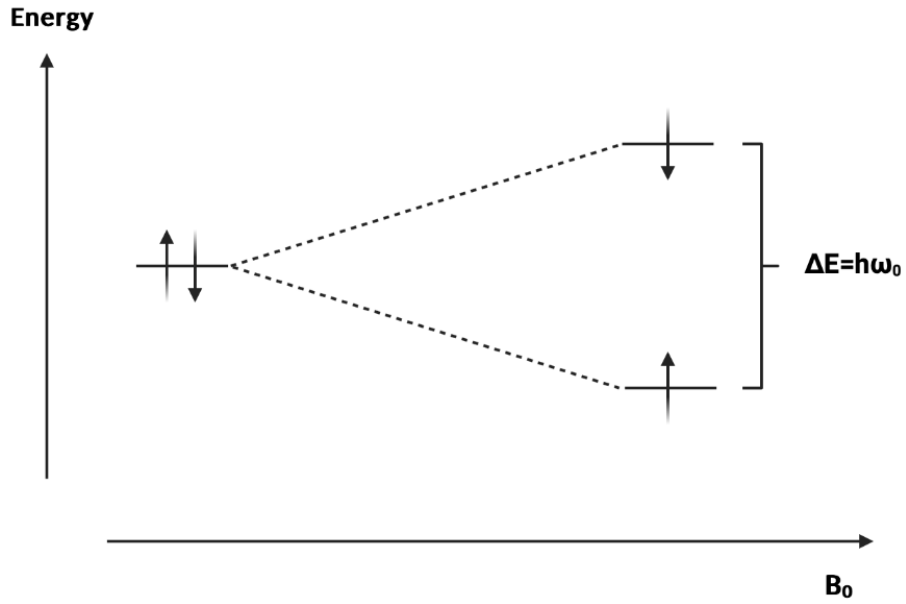


Figure 1: Zeeman effect: splitting of the energy levels of a particle in the presence of an applied magnetic field.

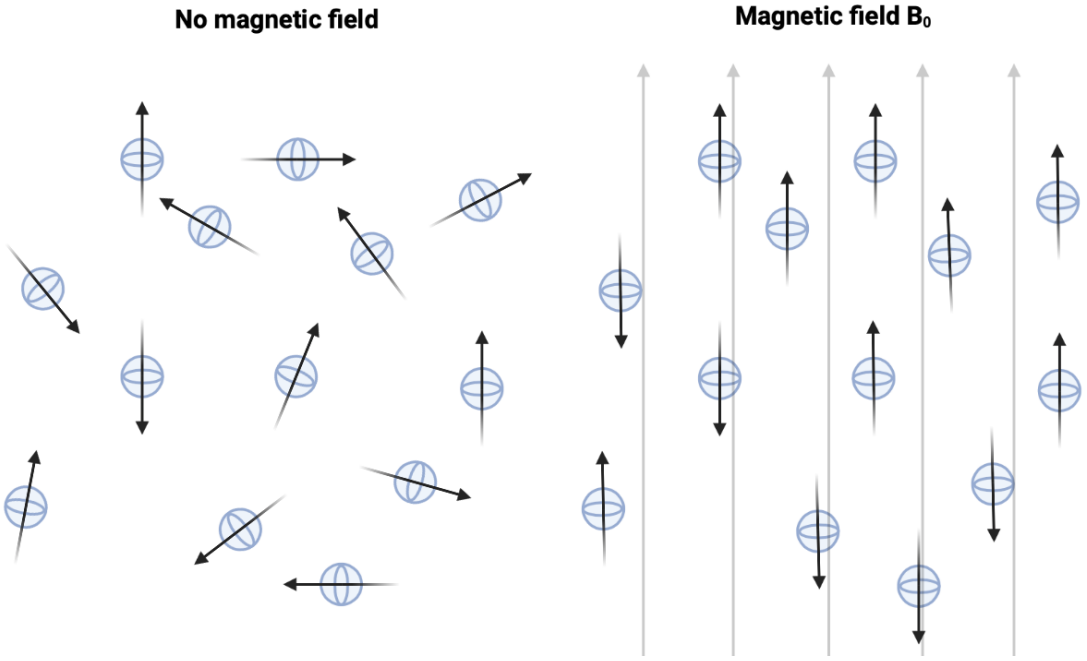


(a) Random directional orientation.

(b) Ordered directional orientation.

Figure 2: Directional distribution of spins (a) without and (b) with the presence of a magnetic field.

The magnetic moment of a particle serves as a measure of its magnetic property and is directly associated with its spin through the equation:

$$\vec{\mu_S} = g\frac{q}{2m}\vec{S} = \gamma\vec{S} \tag{2}$$

Within this equation, $\vec{S}$ represents the particle's spin, $q$ signifies the electric charge of the particle, $m$ represents its mass, and $g$ is the dimensionless g-factor. These parameters collectively contribute to the determination of the gyromagnetic ratio $\gamma$, which serves as a nucleus-specific measure of the particle's spinning frequency.

When a proton is subjected to an external magnetic field, it experiences a torque that arises from the cross product between its magnetic moment and the magnetic field:

$$\vec{\tau} = \vec{\mu} \times \vec{B_0} \tag{3}$$

As a result, this torque exerts a force on the spins, causing them to undergo a precessional motion around the main magnetic field. This interaction between the magnetic moment of a proton and the magnetic field is illustrated in Figure 3. Following an RF-pulse, the torque acts to realign the protons, driving them back to equilibrium and the lowest energy state.

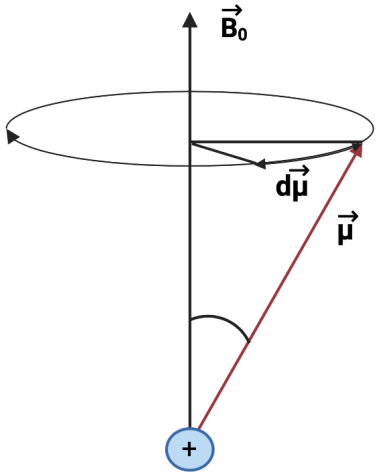


Figure 3: Interaction between an external magnetic field and the magnetic moment of a single proton

The last term in Equation (1) gives rise to the relationship known as the Larmor frequency:

$$\omega_0 = \gamma B_0 \tag{4}$$

This frequency represents the rate at which the spins precess around the magnetic field. The nucleus specific Larmor frequency forms the foundation of MRI, enabling the differentiation of various nuclei based on their distinct precession frequencies.

The MR signal arises from an ensemble of spins. The distribution of spins among the different energy states follows a Boltzmann distribution, expressed as,

$$\frac{N_\uparrow}{N_\downarrow} = e^{-\frac{\gamma h B_0}{2\pi k_B T}} \tag{5}$$

where $N_\uparrow$ and $N_\downarrow$ correspond to the number of spins in the spin-up and spin-down states, respectively. $k_B$ is the Boltzmann constant and $T$ the absolute temperature. The spin-up state, which aligns the protons with the main magnetic field, requires less energy compared to the spin-down configuration. Consequently, there is a higher population of protons in the spin-up state. Equation (5) provides the ratio of spin-up to spin-down populations.

### 2.1.2 MR Components and Image Acquisition

The subsequent section provides a brief overview of the constituent components of the MR system and elucidates their role in the image acquisition process.

The MR scanner is comprised of a strong magnet, a gradient system consisting of three coils, a radio frequency transmitter and receiver, and a computer for regulating and controlling the system. When a patient is placed in the MR scanner, the coordinate system typically used is as follows: the z-axis goes inside the bore of the magnet, the x-axis goes from left to right, and the y-axis from bottom to top of the patient.

The main magnet generates a strong, static magnetic field in the z-direction that magnetizes protons in the tissue. When magnetized, the energy levels are split and the spins will align parallel or anti-parallel to the main magnetic field, as illustrated in Figure 2b. A greater fraction of the spins are aligned parallel and thus generating a magnetization vector in that direction called the longitudinal magnetization vector, $M_z$, highlighted in Figure 4.

When the spins are in equilibrium, the magnetization vector does not produce any signal. Even tough the individual spins precess around the direction of the main magnetic field in equilibrium, summation of their transverse components computes to zero. To produce a detectable signal, the radio frequency coils generate pulses of small magnetic fields, $B_1$, oscillating at the Larmor frequency. The $B_1$- fields transfer energy to the nuclei at resonance, resulting in excitation from spin up to spin down, and simultaneously accomplishing phase coherence. At the macroscopic level, this result in a flip of the magnetization vector away from the z-direction and into the transverse plane, as shown in Figure 4. Immediately after the RF-pulse, the excited nuclei releases energy while relaxing back to equilibrium, and the transverse magnetization vector, $M_{xy}$ diminishes while the longitudinal grows back. The released energy is recorded as a radio frequency signal by the RF coils, and it contains information about the phase, frequency and amplitude of the signal. This is the basis for the MR signal.

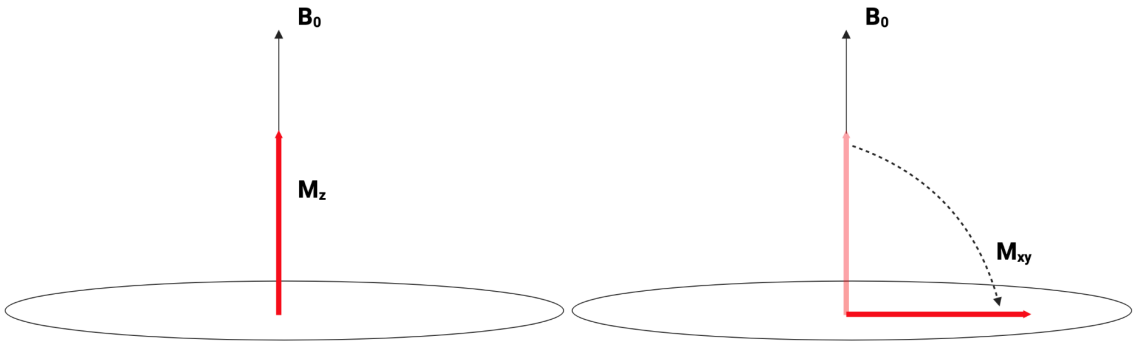


(a) (b)

Figure 4: Illustration of (a) longitudinal magnetization vector in z-direction and (b) flipped transverse magnetization vector in the xy-plane.

The measured signal must be spatially encoded in order to construct a meaningful MR image. Spatial localization of the signal is achieved by utilizing independent and linearly varying magnetic field. The gradient coils produces gradient magnetic fields in the three orthogonal directions x, y and z. Slice selection is achieved by employing a gradient magnetic field along the z-axis during transmission of the excitation pulse. The additional magnetic field will superimpose on the main magnetic filed, resulting in a slightly different Larmor frequency, given by the equation

$$\omega(z) = \omega_0 + \gamma \cdot G_s \cdot z \tag{6}$$

where $G_s$ is the magnitude of the slice selection gradient and $z$ is the position along the axis of the gradient. The phase and frequency of the spins in the excited slice are encoded in a similar fashion.

### 2.1.3 Relaxation Mechanisms

The signal will decay quickly after the RF pulse has flipped the magnetization vector into the transverse plane. The decay of the signal is caused by two relaxation mechanisms known as longitudinal relaxation ($T_1$) and transversal relaxation ($T_2$). The relaxation mechanisms occurs simultaneously, but independently. Due to the distinct molecular composition of different tissue, they exhibit varying relaxation times of $T_1$ and $T_2$. The different relaxation times of different tissues are used to create contrast in the form of $T_1$-weighted images and $T_2$-weighted images.

$T_1$ relaxation refers to the return of the longitudinal magnetization vector after an excitation-pulse has flipped it into the transverse plane. The tissue specific $T_1$ value is defined as the time it takes for the longitudinal magnetization vector of that tissue to return to 63% of its initial value $M_0$. Illustration of the $T_1$ relaxation process are shown in Figure 5a.

$T_2^*$ refers to the diminishing transversal magnetization vector after a RF pulse. There are two causes for the $T_2^*$ relaxation. The first is $B_0$ inhomogeneity, usually denoted by $T_2^{'}$. Magnetic field inhomogeneities caused by hardware limitations and susceptibility variations gives slightly different Larmor frequencies for protons at different locations, resulting in dephasing of the protons in the sample. This effect is reversible by constructing the imaging sequence in a specific way. A spin echo sequence can be utilized to omit the dephasing effect caused by $B_0$ inhomogeneities. The second

effect is caused by stochastic and temporal varying interactions between the magnetic moment of neighboring spins, denoted as $T_2$, [8]. Similarly as for $T_1$, the tissue has a specific $T_2$ value which is defined as the time it takes for the transversal magnetization vector to diminish to 37% of its initial value $M_{xy}$ after a 90° excitation pulse.

$$\frac{1}{T_2^*} = \frac{1}{T_2} + \frac{1}{T_2'} \tag{7}$$

The free induction decay (FID) is the signal measured in the RF coil.

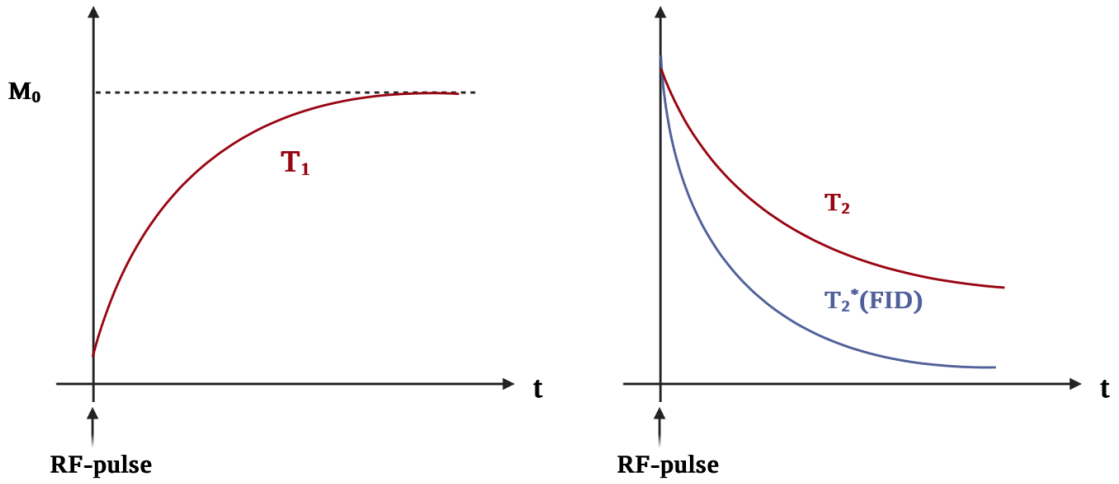


(a) (b)

Figure 5: Illustration of (a) longitudinal relaxation (b) transverse relaxation.

## 2.2 MR Sequences

As mentioned earlier, MRI has the unique ability to generate a large set of different contrasts. A particular type of contrast is achieved by utilizing a specific MR sequence. A MR sequence is a number of RF-pulses, $B_1$, and gradients, $G_{xyz}$, employed in such a way that the image contains certain characteristics, [9]. New MR sequences are constantly being developed, and $T_1$-weighted and $T_2$-weighted are commonly used in MRI. In this thesis, the INV2 image from the $T_1$ - weighted MP2RAGE sequence was used to segment the subjects' cervical spine. A gradient echo sequence was used to compute the phase image that was compared to the simulated field map.

### 2.2.1 Gradient Echo

Gradient echo sequence, also known as GRE, is a fast imaging technique employing low flip angles. The sequence has a wide range of clinical applications, including fMRI, susceptibility weighted imaging and detection of bleeding in stroke patients.

The gradient echo sequence omits the formation of a spin echo and directly uses the signal from the free induction decay. Thus, mechanisms such as field inhomogeneities and susceptibility artifacts are not refocused, as in spin echo sequences, [8]. The measured signal is the FID, as described in Section 2.1.3. $B_0$ field mapping can be performed with a GRE sequence.

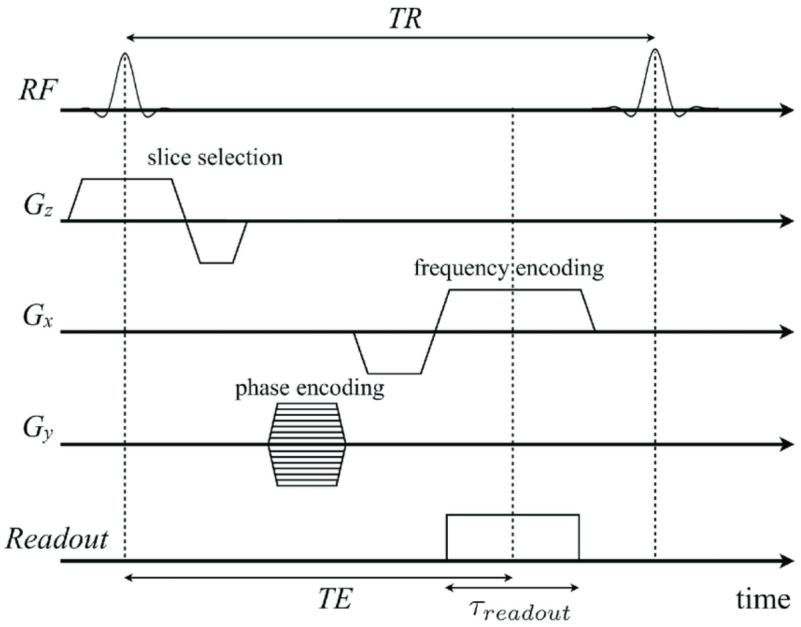


Figure 6: Illustration of a basic gradient echo sequence, acquired from [10]

#### Field Mapping

Gaining insights into the field inhomogeneity within the imaging volume can be accomplished by employing a field mapping imaging sequence. $B_0$ inhomogeneity results in an additional phase accumulation term in the signal, which progressively accumulates over time after RF excitation. The field mapping sequence acquires two images at different echo times while retaining the complex information within them. This complex information enables the extraction of details concerning the additional phase accumulation that transpires between the two echo times. The phase difference

in the signal between the two echo times can be subsequently computed from the equation,

$$\Delta\phi = \angle[S_1 \cdot S_2^*]$$

Let $S_1$ and $S_2$ represent the images obtained at echo times $TE_1$ and $TE_2$ respectively. The superscript $^*$ denotes the complex conjugate of the signal, and $\angle$ indicates the computation of the angle of the complex data. The resulting phase difference will fall within the range of $\pm\pi$. However, it is important to note that the accumulated phase of the signal between the two echo times can exceed this interval of $[-\pi, \pi]$ if the susceptibility-induced field gradient (SFG) is strong enough.

The local frequency shift caused by $B_0$ inhomogeneity is directly proportional to the phase accumulation occurring within the time interval $\Delta TE$. The relation is expressed in Equation (8).

$$\Delta\omega = \frac{\Delta\phi}{\Delta TE} \tag{8}$$

### 2.2.2 MPRAGE and MP2RAGE

MPRAGE (Magnetization Prepared - RApid Gradient Echo) has become the dominant MR sequence for 3D - T1-weighted imaging, and especially on Siemens scanners, since its development 30 years ago. "A typical 3D MP-RAGE sequence uses a three step cycle: 1) a magnetization preparation for contrast control, 2) data acquisition with a short TR gradient-echo sequence and 3) magnetization recovery for additional contrast control ", [11].

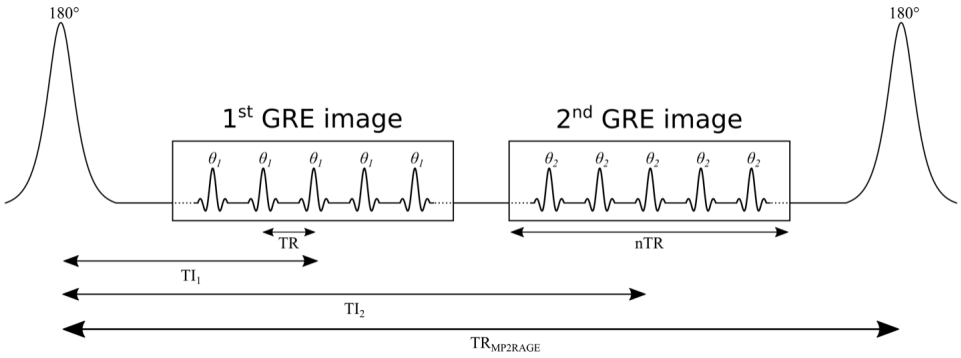


Figure 7: Simplified diagram of a MP2RAGE sequence. Image present [12]

MP2RAGE is a variation of the standard MPRAGE sequence. Following the inversion of the longitudinal magnetization, two images are acquired with a radiofrequency spoiled rapid gradient echo readout train at each of the two different inversion times, [13]. The two images are called INV1 and INV2 from the the two inversion times they are captured. Figure 7 depicts a simplified diagram of the MP2RAGE sequence.

## 2.3 Magnetic Susceptibility

Magnetic susceptibility, $\vec{\chi}$, is an intrinsic and dimensionless quantity that describes a materials tendency to interact with and be magnetized by an external magnetic field, [14]. The amount of magnetization is directly proportional to the applied magnetic field and is given by,

$$\vec{M} = \chi \vec{H}, \tag{9}$$

where $\vec{M}$ is the induced magnetization from the susceptibility distribution and $\vec{H}$ is the applied magnetic field.

At the microscopical level, there are several mechanisms responsible for the amount of susceptibility within a bulk of tissue. In general, $\chi$, arises from the orbital motion of electrons, and the spins of nuclei and electrons in a molecule. The sum of these effects determines the overall susceptibility of a material. The most basic mechanism of susceptibility is caused by the subtle change of motion of electrons around an atom that induces a magnetic field opposing the applied field, a diamagnetic effect, in accordance with Lenz law. This mechanism is present in all materials, but is relatively weak, and in paramagnetic materials it is overridden by more powerful mechanisms, [14].

Because of the different molecular composition of tissue, they exhibit different values of susceptibility. The materials are characterized into three groups based on their susceptibility value: diamagnetic-, paramagnetic- or ferromagnetic materials. Diamagnetic materials have negative susceptibility value and opposes the applied magnetic field. Examples of diamagnetic materials are water, calcium, and most organic materials. Paramagnetic materials have positive susceptibility values and will augment the applied field. Molecular oxygen is the most abundant paramagnetic molecule in the body. Ferromagnetic materials are super paramagnetic and will augment the applied magnetic field substantially. Metals, such as iron, nickel and cobalt are ferromagnetic, and safety protocols prohibit the appearance of such metals near the scanner.

Eq. (9) states that the induced magnetic field from a susceptibility distribution is proportional to the applied magnetic field, [15]. Combining the induced magnetic field with the applied magnetic field gives the local magnetic field, $\vec{B}$ that the spins within a bulk of tissue experience.

$$\vec{B} = \mu_0(\vec{H} + \vec{M}) = \mu_0(1 + \chi)\vec{H} \tag{10}$$

Here $\mu_0$ is the permeability in vacuum. Eq. (10) shows mathematically the effect diamagnetic and ferromagnetic materials have on the local magnetic field. As stated earlier, diamagnetic materials have negative $\chi$, making the local field $\vec{B}$ less than the applied field $\vec{H}$. The opposite effect is true for ferromagnetic materials. While susceptibility variations at a microscopic scale are the source of contrast, a macroscopic susceptibility variations leads to global field inhomogeneities creating off-resonance artefacts, [16].

### 2.3.1 Susceptibility Artifacts

In acquisition of the MR signal, the main magnetic field is assumed to be spatially homogeneous over the sample volume. However, once a subject is placed in the MR scanner, the induced magnetic field from the susceptibility distribution in the tissue distort the uniformity of $B_0$, and violates this assumption. The presence of local inhomogeneity in the magnetic field are the source of image artefacts in the MR-image, in the form of off-resonance artifacts such as geometric distortions and

signal loss, [16]. These local inhomogeneities in the magnetic field are more pronounced at high field strengths, such as 7T. This is because of the linear relationship between field strength and susceptibility, in accordance with Eq.(9).

### 2.3.2 Signal Loss

Local field variations in regions with different susceptibility lead to phase changes. From Eq. (4), the resonance Larmor frequency is proportional to the magnetic field strength. Inhomogeneity in the main magnetic field causes spins in the sample unwanted spatial dependence by altering the locally experienced Larmor frequency, ([17]).

### 2.3.3 Geometric Distortions

As mentioned in Section 2.1.2, a correct sampling of the MR signal in k-space relies on the linear relationship between the proton's position and frequency given by the gradient coils. Macroscopic variations in the field homogeneity will disturb the linearity and give local phase shifts causing the spins to be incorrectly spatially encoded.

### 2.3.4 Shimming of the Main Magnetic Field

Image reconstruction in MRI relies on two crucial assumptions: the uniformity of the main magnetic field ($B_0$) and the linearity of the gradients [18]. Uniformity of the $B_0$ field is vital for achieving high-quality images, while inhomogeneities can lead to artifacts such as geometric distortions and signal loss. Magnetic field homogeneity is commonly measured in parts per million (ppm) difference from the desired $B_0$ value [19]. Inhomogeneity increases proportionally with the main magnetic field strength. For instance, a 1 ppm deviation on a 7T magnet corresponds to a 7 $\mu$T deviation in the magnetic field.

To meet the strict uniformity requirement, MR scanners are manufactured with a static magnetic field deviation of less than 1 ppm [16]. During installation, the magnetic field of the scanner is adjusted through a process called shimming to achieve this level of homogeneity.

Shimming is a technique used to optimize the $B_0$ homogeneity in MRI. It involves applying external fields to approximate and counteract local field distortions [20]. Shimming techniques fall into two broad categories: passive and active shimming.

Passive shimming is performed during installation by strategically placing materials with specific magnetization properties to mitigate $B_0$ inhomogeneity. However, individual variations in patients' characteristics introduce additional magnetic field distortions, necessitating the use of patient-specific shimming techniques.

Active shimming, on the other hand, utilizes specialized coils called shim coils. These coils have adjustable electric currents running through them, generating their own magnetic fields to fine-tune the main magnetic field [19, 18]. This dynamic approach allows for precise adjustments and compensation for individual variations, resulting in improved image quality during MRI examinations.

## 2.4 Segmentation

Segmentation is the process of classifying pixels within the same region of interest (ROI). Typically, the ROI is an organ, tumour or a type of tissue. In medical image analysis, segmentation plays a pivotal role and serves as the foundation for various applications. In the context of MRI, segmentation is commonly utilized to measure and visualize anatomical structures within the brain, [21].

Over the past few decades, diverse segmentation techniques with varying levels of accuracy and complexity have been developed. With the advent of artificial intelligence, future segmentation methods hold the potential to deliver faster and more precise results compared to existing approaches.

Among the commonly employed segmentation techniques are classification, thresholding, edge attraction, and clustering. Classification is a simple, semi-automatic segmentation method where different tissues or organs (ROIs) are classified with specific labels. Thresholding is a common automatic segmentation method. Pixels or voxels are classified based on their intensity values being above or below a specified threshold. This method is particularly effective for segmenting bright objects on dark backgrounds, [22]. Edge detection, on the other hand, aims to identify sudden intensity transitions between neighboring pixels or voxels. Clustering, an unsupervised learning method, entails categorizing voxels into a finite set of clusters. In the case of brain segmentation, one might classify white matter and gray matter as distinct clusters. This grouping is achieved by defining a similarity criterion between voxels and maximizing the inter-class similarity during the clustering process , [22].

Most segmentation software are primarily developed for CT image segmentation or for brain MRI segmentation. When searching for suitable segmentation software, a review article by Virzi et al. (2020) titled *Comprehensive Review of 3D Segmentation Software Tools for MRI Usable for Pelvic Surgery Planning*, [2], was utilized as a valuable reference for guidance in the selection process.

## 2.5 Modelling the Susceptibility-Induced Field

A sample described by a magnetic susceptibility distribution, $\chi(\vec{r})$, exposed to an external magnetic field, $B_0$, induces field distributions given by

$$\vec{B}(\vec{r}) \approx \vec{B}_d(\vec{r}) = \frac{\mu_0}{4\pi} \int_V \frac{1}{\left|\vec{r} - \vec{r'}\right|^3} \cdot \left( 3\frac{\vec{M}(\vec{r'}) \cdot (\vec{r} - \vec{r'})}{\left|\vec{r} - \vec{r'}\right|^2} (\vec{r} - \vec{r'}) - \vec{M}(\vec{r'}) \right) d^3r', \tag{11}$$

where $\vec{M}$ is the magnetization distribution given by the susceptibility distribution. Eq. (11) is obtained by solving Maxwell's equations with a first-order dipole approximation, ([4, 23]).

Normally in MR, the main magnetic field is applied in the z-direction, and it is only in this direction the induced magnetization of the material differs significantly from zero. That is why we only consider the magnetization in z-direction, ([4]), which can be expressed as

$$M \approx M_z(\vec{r}) = \chi(\vec{r}) \frac{B_0}{\mu_0 \mu_r(\vec{r})} = \chi(\vec{r}) \frac{B_0}{\mu_0(1 + \chi(\vec{r}))} \approx \chi(\vec{r}) \frac{B_0}{\mu_0} \tag{12}$$

The approximation is based on the assumption that $|\chi| \ll 1$, which generally is true when imaging the human body, [5]. The induced magnetic field generated from a susceptibility point at a position, $\vec{r}$, by the resulting magnetization distribution is a complicated function, representing the sum of the dipole fields generated by each element of the magnetization distribution, $\vec{M(r')}$. The z-component of the normalized magnetic field, $\vec{B_{z,d}}/B_0$, can be obtained by inserting Eq. (12) into Eq. (11). This gives

$$\frac{\vec{B_{z,d}}(\vec{r})}{B_0} = \frac{1}{4\pi} \int_V \left( 3\frac{\vec{\chi}(\vec{r'}) \cdot (z - z')^2}{\left|\vec{r} - \vec{r'}\right|^5} - \frac{\vec{\chi}(\vec{r'})}{\left|\vec{r} - \vec{r'}\right|^3} \right) d^3r' \equiv \int_V \vec{\chi}(\vec{r'}) D_z(\vec{r} - \vec{r'}) \tag{13}$$

Where the last part of the expression introduces the z-component of the unit dipole field, $D_z$, given by

$$D_z(\vec{r}) = \frac{1}{4\pi} \left( \frac{3z^2 - |\vec{r}|^2}{|\vec{r}|^5} \right) = \frac{1}{4\pi} \left( \frac{3 \cdot cos^2\theta - 1}{|\vec{r}|^3} \right) \tag{14}$$

where $\theta$ is the angle between $B_0$ and $\vec{r}$. The last part of Eq. (13) shows that the normalized field in the z-direction is the convolution of the susceptibility distribution, $\vec{\chi}(\vec{r})$ and the dipole function, $D_z(\vec{r})$ given in Eq. (14). The convolution theorem, stating that convolution of two functions in one space is multiplication of the same functions in Fourier space, that is k-space. The expression from Eq. (13) reduces to

$$\frac{\vec{B_z}(\vec{k})}{B_0} = \vec{\chi}(\vec{k}) \times D_z(\vec{k}) \tag{15}$$

Taking the 3D Fourier transform of Eq. (14) gives the dipole field in k-space as

$$D_z(\vec{k}) = \left( \frac{1}{3} - \frac{k_z^2}{k_z^2 + k_x^2 + k_y^2} \right) \tag{16}$$

The dipole field is shown in the Figure 8.

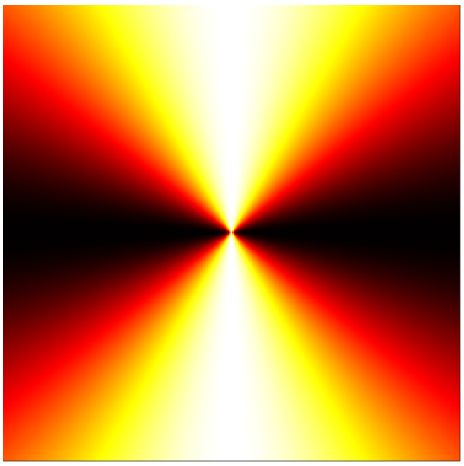

Figure 8: Simulated dipole kernel, $D_z(\vec{k})$, in $k$-space.

## 2.6 UHF MRI of the Spinal Cord

The objective of this thesis is to segment the cervical spine and evaluate the induced magnetic field resulting from the susceptibility distribution within the cervical spine. This section presents a concise overview of the cervical spine, its functions, and the challenges associated with performing MRI of the spinal cord at high magnetic field strengths.

The cervical spine consists of seven vertebrae, known as C1 through C7. Its primary functions are to protect the spinal cord, support the skull, and facilitate movement of the head and neck. In Figure 9, the left side highlights the cervical spine in green, while the right side illustrates the typical structure of a cervical vertebra.

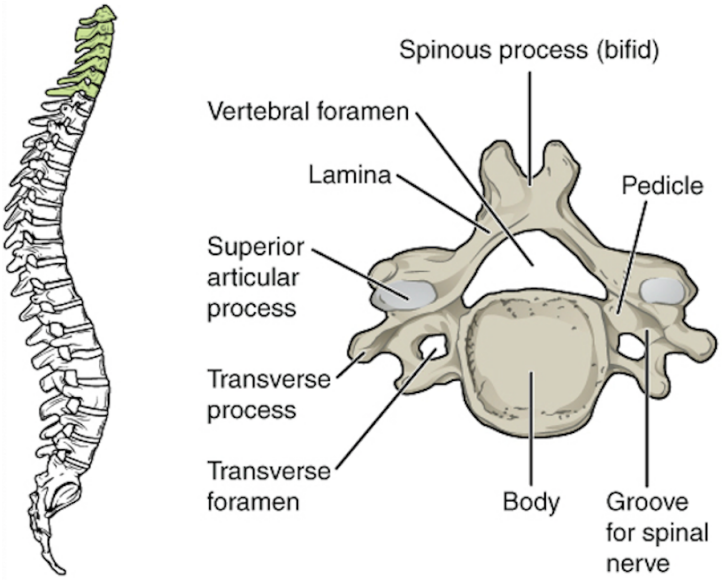


Figure 9: Structure of cervical vertebrae. Case courtesy of OpenStax College, Radiopaedia.org, rID: 42770

The vertebrae in the cervical spine are stacked on top of each other, with intervertebral discs between them that act as shock absorbers. The body of each vertebra faces the throat, while the spinous process is located on the backside of the neck. The spinal cord, an integral part of the central nervous system, extends from the head to the middle of the back through an aperture in the vertebrae called the vertebral foramen or spinal canal. Surrounding the spinal cord is cerebrospinal fluid (CSF), which is protected by membranes. The outermost membrane, known as the "dura mater," encloses the spinal cord and prevents leakage of CSF. Additionally, there are two openings called transverse foramina on each side of the main body of the vertebrae. These foramina house nerve roots and blood vessels, as described by Nógrádi et al. [24].

MRI of the spinal cord is particularly challenging due to susceptibility variations among different tissues present, including vertebrae, muscle, cerebrospinal fluid (CSF), grey and white matter, fat, and even air in the lungs. These variations in susceptibility result in rapidly changing magnetic field distortions, significantly affecting the applied magnetic field, as highlighted by Saritas et al. [16]. This thesis aim to study the induced magnetic field distortions in the spinal column, caused by the susceptibility distribution in the cervical spine.

# 3 Methods

Experimental data for this thesis was acquired on the 7T Siemens MAGNETOM Terra scanner located at St. Olav's hospital in Trondheim, Norway. The signal was acquired with a 1Tx/24Rx-$^1H$ cervical spine coil from MRI.TOOLS GmbH. The acquired DICOM images were converted to NiFTi files using dcm2niix, [25]. All simulations were implemented and performed in Matlab R2021b (The Mathworks Inc., Natick, MA), on a Macbook Pro with 2.4 GHz Dual-Core Intel Core i5 and with 8 GB usable RAM. The main functions used for the simulations are found in Appendix A. In total, seven female subjects in their mid 20s were imaged. The images of the first two subjects were discarded due to too poor contrast from weak measured signals.

## 3.1 Segmentation

MP2RAGE images were taken of the subjects and used for segmentation. The images had a FOV of 242 mm × 192 mm × 368 mm and a resolution of 0.71 mm × 0.70 mm × 0.71 mm. The repetition time (TR) and the echo time (TE) was set to 5000 ms and 2.15 ms, respectively, and the inversion times, TI1 and TI2, for the two images in the sequence were 0.7 s and 2.4 s. The segmentations were obtained from the INV2 images, corresponding to TI2. In this thesis, the segmentation software ITK-SNAP, [26], was chosen to segment the MR images. The review article titled *Comprehensive Review of 3D Segmentation Software Tools for MRI Usable for Pelvic Surgery Planning*,[2], ranked ITK-SNAP as the overall best choice for segmentation of MRI. Based on this ranking, the software was tested and chosen based on the following: availability of several segmentation techniques, possibility of visualizing the segmentation as a 3D model, and last but not least its simplicity and user-friendliness.

### 3.1.1 ITK-SNAP

ITK-SNAP is a free, open-source, multi-platform software application used to segment structures in 3D and 4D biomedical images, [26]. The software is made specifically for segmentation of medical images, and has easy-to-use manual, semi-automatic, and automatic segmentation methods. All of the segmentation techniques described in Section 2.4 are available in ITK-SNAP.

#### Manual Segmentation

From each subject, a manual segmentation was obtained through the "paint" method. The segmentation of the cervical spine involved meticulously analyzing every slice in the sagittal, coronal, and transverse planes of the MR image. In each slice, the dark regions assumed to correspond to the cervical spine were manually painted. This comprehensive process covered the parts of the matrix containing the cervical spine, in the three planes. Figure 10 shows the sagittal view and the 3D model when segmenting in ITK-SNAP.

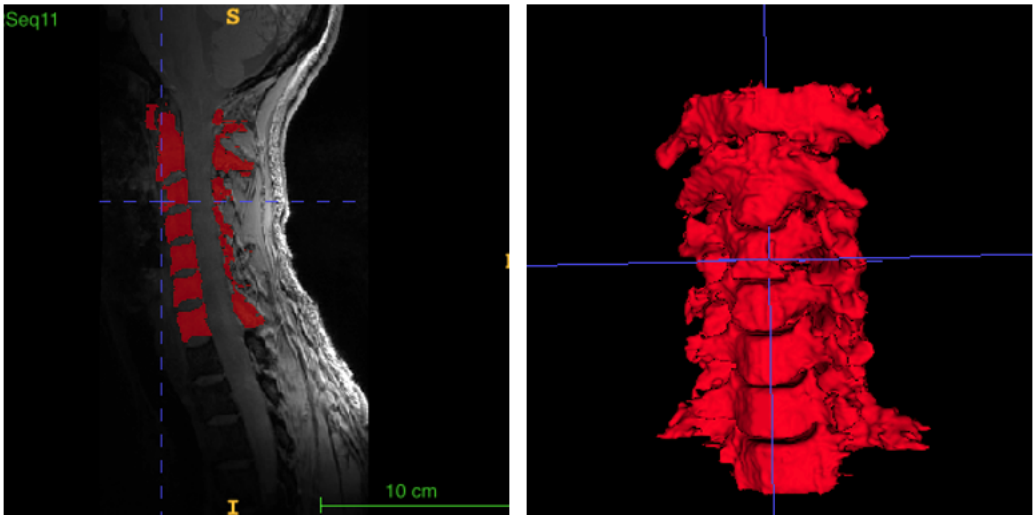


Figure 10: Layout of ITK-SNAP when doing manual segmentation. The red color is the applied segmentation. To the left, the sagittal view, and to the right, a zoomed in view of the 3D model.

### Semi-Automatic and Automatic Segmentation

ITK-SNAP has several features for semi-automatic and automatic segmentation. The two choices for fully automatic segmentation is the thresholding method and the edge detection method, as described in Section 2.4, and the semi-automatic methods are classification and clustering. The classification method and the thresholding method was used for segmentation in this thesis. The other two methods were tested, but the resulting segmentation was poor. A comparison was conducted through visual assessment and by quantitative evaluation. A box was placed in the image volume to define the segmentation region, depicted in Figure 11. The box remained fixed for both segmentation techniques, in order to make the comparison valid.

Figure 11: Image depicting the box (red, dashed lines) used in semi-automatic and automatic segmentation.

### Quantifying the Semi-Automatic and Automatic Segmentation Techniques

In the following discussion, manual segmentations are assumed to represent the gold standard. In the segmentation box used for the (semi-)automatic segmentations, the voxels corresponds to either true positives (TP), false positives (FP), true negatives (TN) or false negatives (FN). These four categories are visualised in Figure 12, for the second subject. In the figure, the manual segmentation is shown on the left for comparison. The middle image represents the voxels classified as true positives. The image to the right shows the false positives in black and the false negative in white, resulting from subtracting the segmentation method from the manual segmentation.


Figure 12: Visual representation of match and mismatch of segmentation method. From left to right a) manual segmentation, b) matrix of TP, and c) matrix of FP (black) and FN (white).

To evaluate the performance of the (semi-)automatic segmentation, the manual segmentation was element-wise multiplied with the (semi-)automatic segmentation, resulting in a matrix that represents the correctly segmented voxels, referred to as true positives in statistical terms. To get the sensitivity of the segmentation method, the matrix containing true positives was summed and divided by the sum of the manual segmentation, as described by the equation below,

$$sensitivity = \frac{TP}{P}$$

Additionally, the (semi-)automatic segmentation were subtracted from the manual segmentation, generating a matrix containing false positive segmented voxels and false negative voxels. The false positive voxels are voxels not corresponding to the cervical spine that the method incorrectly segmented, and the false negative voxels are voxels corresponding to the cervical spine that were not segmented by the method. These values were used to calculate the true negative values of the method in order to obtain the specificity of the segmentation method. The specificity is given in the equation below, and is a measure of the probability of the method to not segment voxels not belonging to the cervical spine. The true negatives were calculated by subtracting the true positives, true negatives and false positives from the total volume of the segmentation box.

$$specificity = \frac{TN}{N}$$

The Dice-Sørensen coefficient were calculated for both segmentation method for all the subjects. The coefficient, abbreviated DSC, is a measure of the overall similarity between two samples, and is calculated by

$$DSC = \frac{2TP}{2TP + FN + FN}$$

## 3.2 Simulated Field Map

A program written by a former master student at the Institute of Physics was used to simulate the induced magnetic field from the segmentation obtained from each subject, [27]. The program is based on the electromagnetic theory described in Section 2.5, and can be found in Appendix A.

A finished segmentation, shown to the right in Figure 10, was imported into Matlab. The segmentation was assigned a susceptibility value of 0.19 ppm, in accordance with the difference between the susceptibility value in bone and the soft tissue surrounding it, [14]. The three views of the segmentation are shown in Figure 13, below.

Figure 13: Slices from the three different planes are shown. From left to right, the transverse plane, the coronal plane and the sagittal plane.

The step-wise process used in the simulation is illustrated in Figure 14. To begin, the segmentation is placed within a larger matrix of size 300 x 300 x 300 before proceeding with the algorithm. In the first step, the imported segmentation undergoes a Fourier transformation into k-space, as indicated by the arrows. Within k-space, the segmentation is multiplied by the dipole field, resulting in the second-to-last image shown in Figure 14.

In the final step, the product of the segmentation and dipole field is inverse Fourier transformed back into image space, producing the simulated field map represented on the right side of Figure 14. This process allows for the creation of the simulated field map based on the segmentation of the cervical spine and enabling further analysis and comparison with the measured field maps.

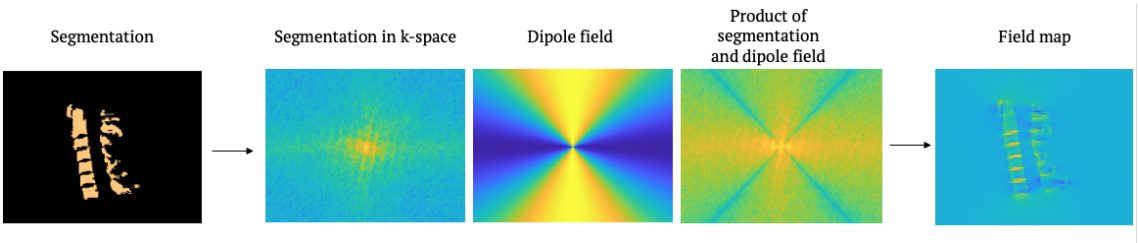


Figure 14: Visual representation of the steps in the algorithm. The first arrow indicates a Fourier transformation, while the second arrow indicates a inverse Fourier transformation.

The simulated field map was scaled using the magnetic field strength, $B_0 = 7\text{T}$, and the gyromagnetic ratio, $\gamma = 42.6$ MHz/T, in order to convert the values to frequency units. This transformation facilitated a meaningful comparison between the simulated field map and the measured frequency offsets, as both datasets were then represented in the same frequency domain.

## 3.3 Measured Frequency Offset

Phase images from each subject were acquired by a GRE sequence. The GRE sequence had a FOV of 190 mm × 190 mm × 20 mm, and a resolution of 1.0526 mm × 1.0526 mm × 2.4 mm. From the sequence, two anatomical images from different echo times were subtracted to yield the phase image. The left part of Figure 15 is one of the anatomical images, and the right show the phase image. The two magnitude images had a TE of 3.1 ms and 4.1 ms. The phase image was scaled, according to Eq. (8) to present the magnetic field map in the imaging volume. This field map, measured on the scanner, was used as a reference in comparison to the simulated field map from the segmentation.

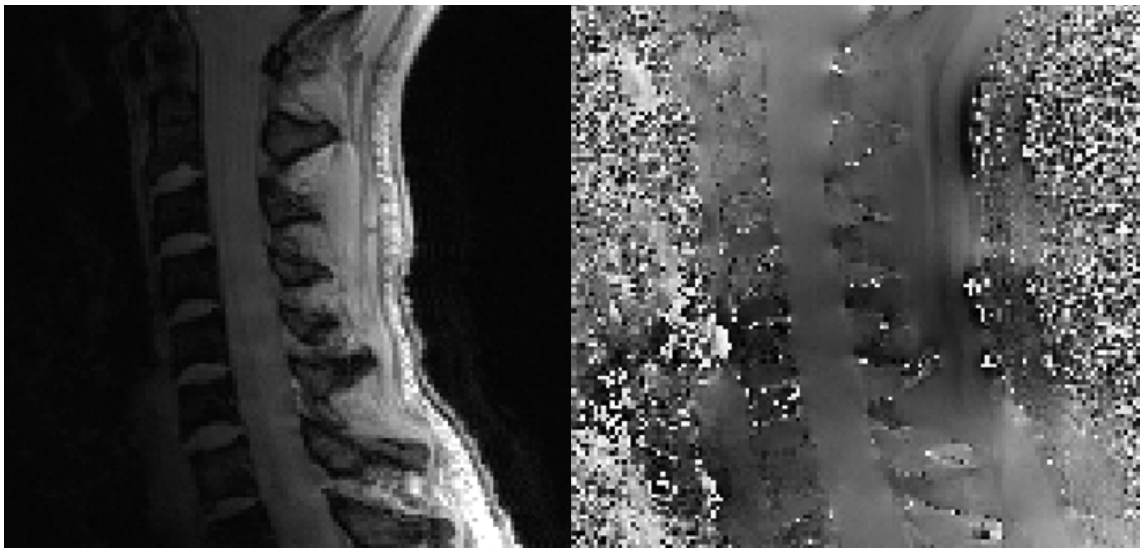

Figure 15: To the left a) anatomical magnitude image and to the right b) phase image from the $B_0$ sequence of the first subject.

The original aim was to use the segmentations obtained from the MP2RAGE sequence to simulate inhomogeneity field maps. However, the images were from different measurements, facilitating the possibility of movement of the subjects. Instead, segmentations of the cervical spine from the magnitude images of the field map acquisition, Figure 15 a), was utilized to simulate induced field distributions from the cervical spine. This ensured similarity between the models and made a direct comparison much easier.

Additionally, a segmentation of the spinal column between the C3 and C5 vertebrae was obtained from the magnitude image. This segmentation served as a placeholder to store measured and simulated field values from the spinal column, allowing for a direct comparison of the simulated and measured fields during the linear regression analysis. By using this procedure, the field maps could be compared from the same volume in the image, ensuring consistency.

To quantify the relationship between the simulated and measured field maps, a linear regression fit was carried out using the Matlab function *polyfit*. This analysis helped determine the extent to which the simulated field maps aligned with the measured field maps, providing valuable insights into the accuracy of the simulation.

## 3.4 Gradient Fields

To asses the directional change in the field map in the z-direction, gradient field maps were calculated. This was done by subtracting adjacent voxels along the z-direction, leaving the difference between the frequency values of neighboring voxels. Gradient field maps in the z-direction were calculated both for the simulated frequency map and the measured frequency map from the MR scanner. To remove the effects in the cervical vertebrae, seen as yellow features in Figure 16, a mask obtained from segmenting the cervical spine from the GRE sequence was multiplied with the gradient field maps.

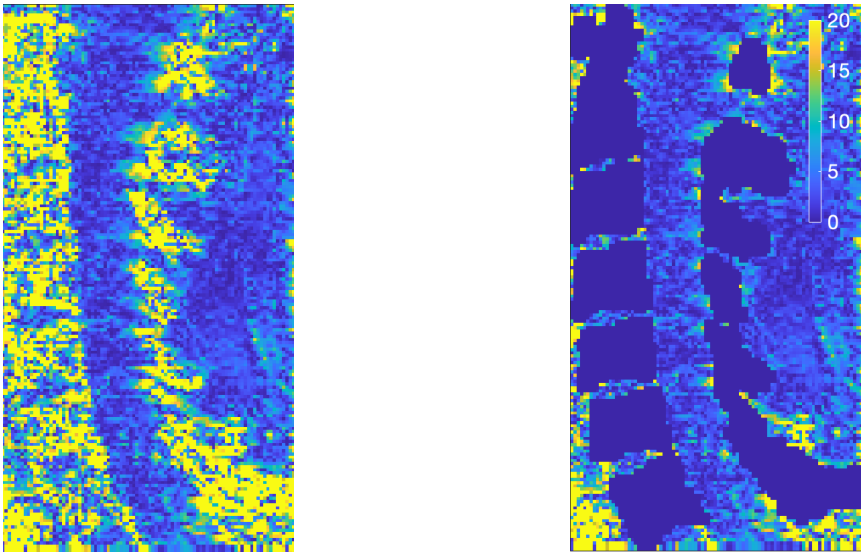


Figure 16: Masking of the gradient in the z-direction of the measured field offset.

# 4 Results

I will begin this chapter by emphasizing segmentation and show the results from a comparative analysis between manual, semi-automatic and fully automatic segmentation methods. Manual segmentation serves as the benchmark for comparison against the other methods used, ensuring a reliable reference point. The time consumption is another parameter to compare. While manual segmentation is a time-consuming process, taking several hours to complete, the semi-automatic and automatic segmentation methods are much quicker, in the order of minutes.

In the second part of this chapter, the $B_0$ inhomogeneity field maps, scaled to frequency offsets ,will be highlighted. The measured frequency offsets acquired at the scanner will be compared to the simulated frequency offsets from the segmentations. A quantitative analysis was performed through regression analysis of the values in the spinal canal between the C3 and C5 cervical vertebrae.

## 4.1 Comparison of Segmentation Methods

In Figure 17, the segmentations of the cervical spine from the second subject are highlighted. The selection of the displayed slices was purposefully made to demonstrate both the regions where the semi-automatic and automatic methods performed effectively and where its performance is comparatively weaker.

The classification method and the thresholding method was used for the semi-automatic and the automatic segmentation, respectively. Segmentations from both methods are placed next to a manual segmentation to make the comparisons direct.

The segmentations from the other subjects are placed in Appendix B at the end of the thesis. The figures for each subject consists of four columns and three rows. The columns corresponds to, from left to right, a) the MR image, b) the manual segmentation, c) the semi-automatic segmentation, and d) the automatic segmentation. The rows presents from top to bottom the sagittal, transversal and coronal plane.

The manual segmentation serves as the reference for comparison and analysis. By comparing Figure 17 a) and b), it is evident that the manual segmentation aligns well with the cervical spine in the MRI. The vertebrae bodies exhibit clear delineation, facilitating their manual segmentation. This is exemplified by the accurate manual segmentation of the vertebrae bodies. However, the spinous processes, visible in the MRI, are not as distinct as the vertebrae bodies. Consequently, the smaller components of the cervical spine pose greater challenges for manual segmentation. Discrepancies between the manual segmentation and the MRI are particularly noticeable in the spinous processes when observing the sagittal and transverse planes. These findings are common for all the subjects.

A common feature when segmenting using the classification or thresholding method, is the poor segmentation in the anterior part of the cervical spine. The methods have difficulties in distinguishing the soft tissue adjacent to the vertebral bodies and the vertebral bodies themselves. This results in ”over-segmentation” in these regions. In Figure 17, this can be seen in all of the planes for the (semi-)automatic segmentations.

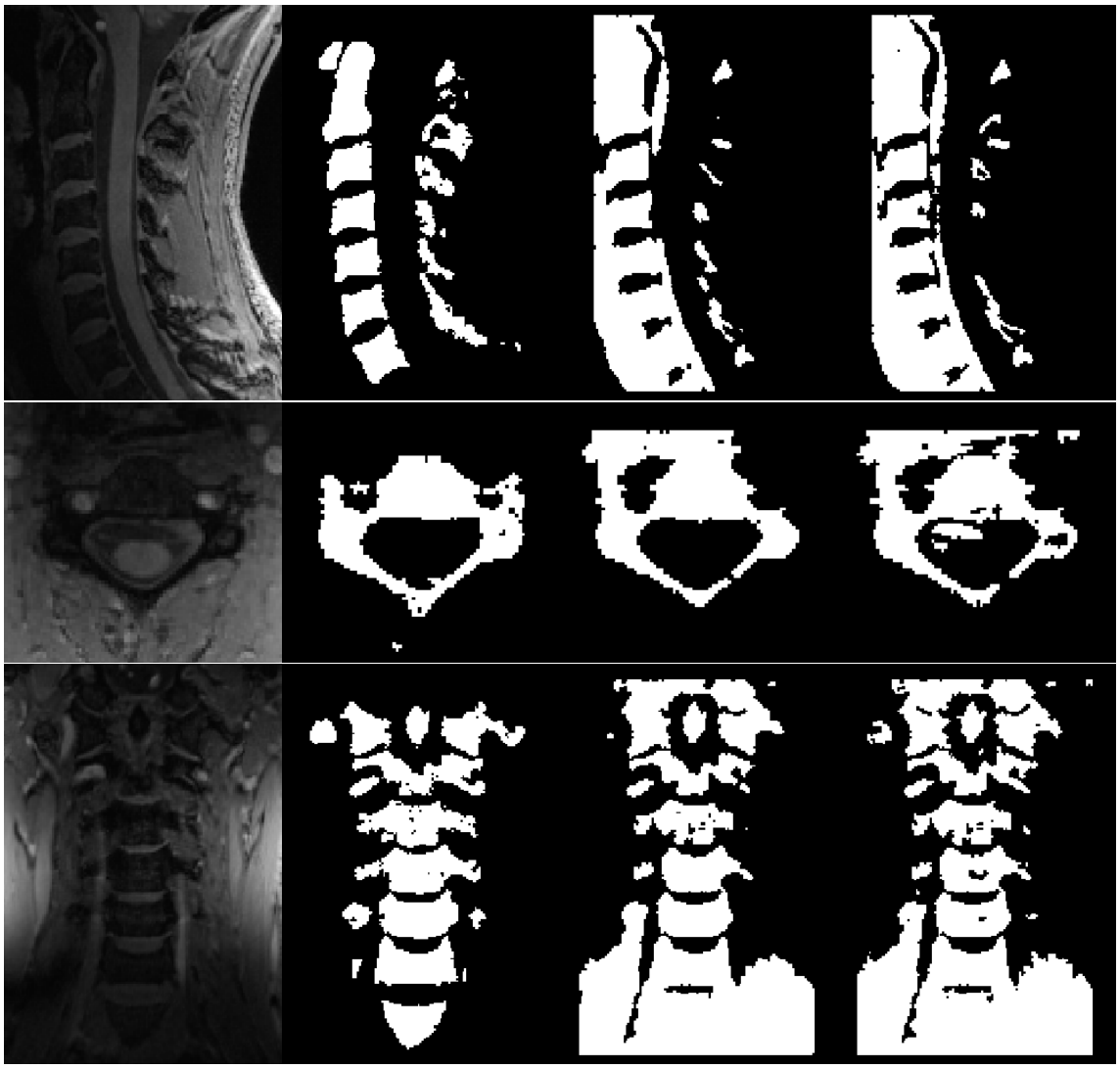

Figure 17: Comparison of segmentations from different methods. From left to right: a) MRI, b) manual segmentation, c) semi-automatic segmentation, and d) automatic segmentation. Top to bottom, the sagittal plane, the transverse plane and the coronal plane.

### Quantification of the Segmentation Methods

A comparative analysis was conducted to assess the accuracy of both the semi-automatic and the automatic segmentation methods in comparison to the manual segmentation. A summary of the findings is presented in Table 1.

The column named *Sensitivity* indicates the proportion of cervical spine the specific method accurately segmented. For instance, for the first subject the classification method segmented 77% of the cervical spine segmented manually. The *Specificity* column is a measure of the probability of the method to not segment voxels not belonging to the cervical spine.

A better measure of the success of the segmentation methods are the Dice-Sørensen coefficient, indicated in the column *DSC*. The DSC is also known as the F1 score. This coefficient measures the overall similarity between two samples. Generally, a similarity above 0.8 indicates a good match, while a score below 0.5 is not good. None of the (semi-)automatic segmentations have a DSC above 0.6, and several have values below 0.5.

| Subject | Semi-Automatic | | | Automatic | | |
|---|---|---|---|---|---|---|
| | Sensitivity | Specificity | DSC | Sensitivity | Specificity | DSC |
| 1 | 0.77 | 0.80 | 0.46 | 0.89 | 0.75 | 0.46 |
| 2 | 0.81 | 0.85 | 0.43 | 0.83 | 0.84 | 0.42 |
| 3 | 0.88 | 0.83 | 0.59 | 0.80 | 0.79 | 0.50 |
| 4 | 0.68 | 0.92 | 0.58 | 0.89 | 0.75 | 0.46 |
| 5 | 0.77 | 0.82 | 0.56 | 0.83 | 0.76 | 0.51 |
| Mean | 0.78 | 0.84 | 0.52 | 0.85 | 0.78 | 0.47 |
| STD | 0.07 | 0.05 | 0.07 | 0.04 | 0.04 | 0.04 |

Table 1: Table of quantitative comparison of the semi-automatic and the automatic segmentation in regard to the manual segmentation.

Figure 18 depicts the manual segmentation next to the automatic segmentations. The (semi-) automatic segmentations were subtracted from the manual segmentation to visualize where the methods correctly segmented and regions where the method failed. As the colorbar indicates, the black parts corresponds to voxels where the automatic segmentations segmented unwanted areas, and the white parts are voxels belonging to the cervical spine that the methods failed to segment. A common feature of the (semi-)automatic segmentation methods are their tendency to segment falsely positive voxels.


Figure 18: Visualization of match and mismatch between the manual segmentation and the automatic segmentation for the second subject.

## 4.2 Field Offset

The result of the regression between the simulated frequency offsets and the measured frequency offsets are shown in Figure 19. In this plot, the scattering of the simulated and measured values for each subject is depicted together, emphasizing the similarity in the slope of the regression line and the distribution of the scatter points. The offset and slope from the linear regression are provided in Table 2. These values offer valuable insights into the degree of agreement between the simulated and measured frequency offsets, allowing for a comprehensive assessment of the susceptibility value assigned in the simulation. The mean value of the slopes are -6.75, with a standard deviation of 0.73. The offset is determined from the demodulation frequency set during the MRI scanning, and has little physical importance in this study. Multiplying the slope with the assigned susceptibility value, 0.19 ppm, yields the difference in susceptibility between bone and soft tissue measured at the scanner. That is, if the segmentation were assigned a susceptibility difference of -6.75·0.19 ppm = -1.28 ppm, the simulation would be a best least square fit to the measured values.

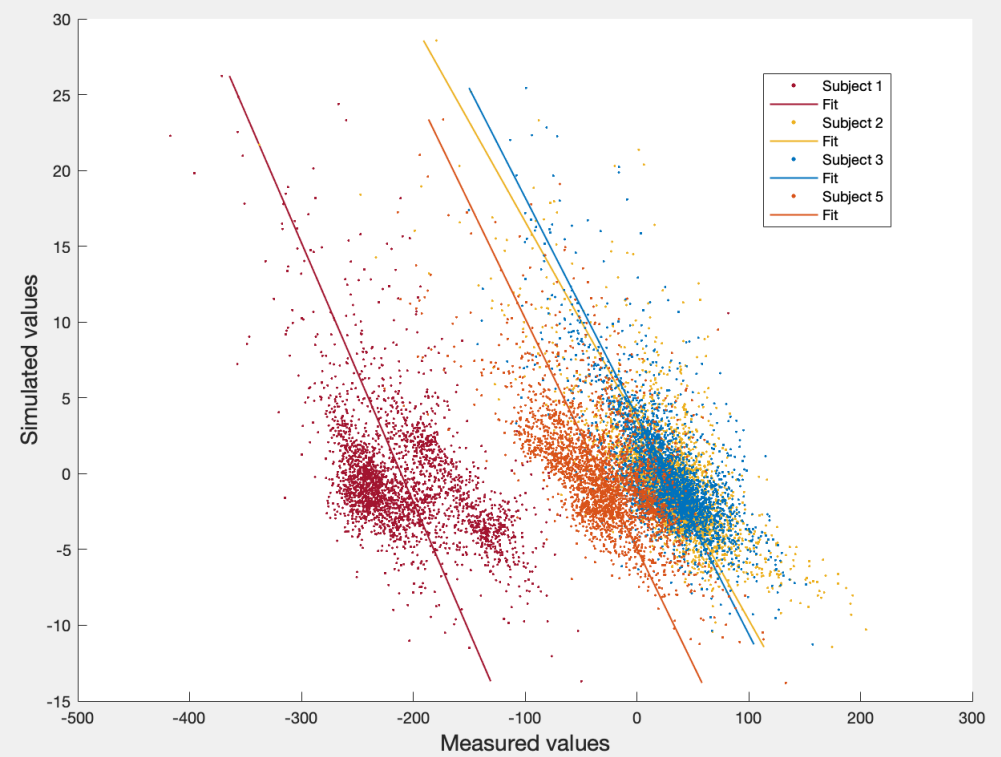


Figure 19: Regression analysis between the simulated field offsets and the measured field offsets from all subjects.

| Subject | 1 | 2 | 3 | 5 | Mean | STD |
|---|---|---|---|---|---|---|
| Offset | -210.87 | 26.62 | 26.51 | -32.56 | - | - |
| Slope | -5.85 | -7.61 | -6.94 | -6.58 | -6.75 | 0.73 |
| Susceptibility difference (ppm) | -1.11 | -1.44 | -1.32 | -1.25 | -1.28 | 0.14 |

Table 2: Table showing the result of the least square regression fit between the simulated and the measured field offsets.

Figure 20 depicts the measured frequency offset to the left, and the simulated frequency offset to the right for the second subject. Field maps for the other three subjects are placed in Appendix C. Two slices taken 10 slices or 7 mm apart are depicted on top of each other to highlight the similar effects between the measured and simulated field throughout the imaging volume. The simulated frequency offset is scaled according to the result of the least square fit model. The color bar on the right hand side is valid for both of the images, and is expressed in units of hertz (Hz).

Several similar features can be seen in the figure. Dipole effects are present both around the spinal process and the vertebral bodies. The effect is especially visual in the spinal process of C1. In the spinal canal, altering positive and negative values can also be seen. This effect is present for all the subjects.

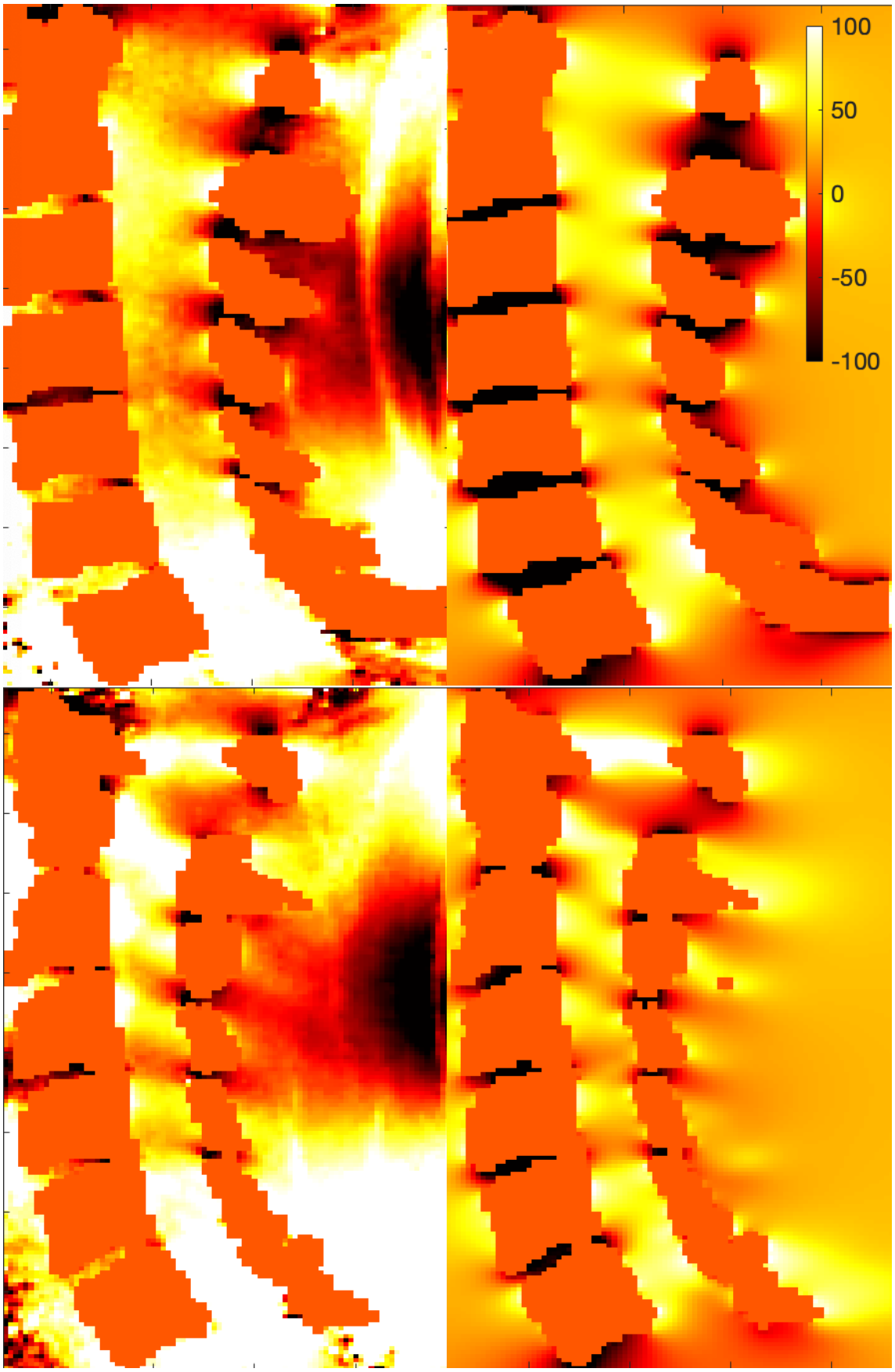


Figure 20: Illustration of a) the measured frequency offsets and b) the simulated frequency offsets from the segmentation. The color bar in the top right corner is valid for the entire figure.

### 4.2.1 Gradient

The result from the calculated gradient frequency offset in the z-direction from the second subject is depicted in Figure 21. The color bar in the right hand corner is valid for both images and is expressed in units of Hz/mm. The measured gradient map is very noisy, making the comparison difficult. However, the dipole effect can be seen around the spinal process, especially around the C1 vertebrae.

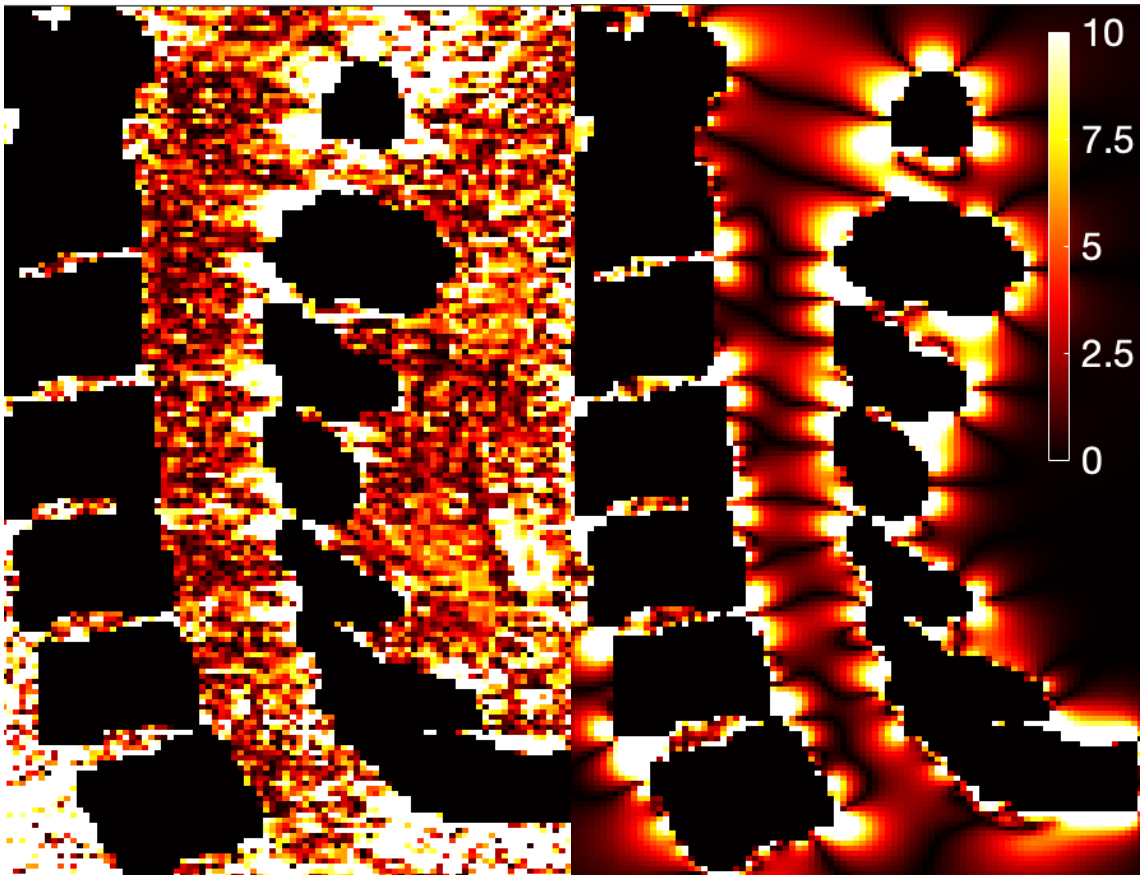


Figure 21: Visualization of the calculated in-plane gradients in the z-direction from a) the scanner and b) the simulated field.

# 5 Discussion

In this thesis, segmentation of the cervical spine was obtained to model induced $B_0$ field distortions in the spinal canal from the susceptibility distribution in the cervical spine. The MRI sequence MP2RAGE was utilized for high resolution anatomical imaging of the cervical spine, and the segmentation software ITK-SNAP was deployed for segmenting the cervical spine. Three different segmentation methods were performed to obtain a mask of the cervical spine: a manual segmentation obtained from painting, a semi-automatic segmentation using classification, and a fully automatic segmentation using thresholding.

Segmentation of the cervical spine from 7T MRI was proven to be possible. The best results were the manual segmentations, which were used as the gold standard in comparison to the (semi-)automatic segmentation methods. The manual segmentations are, however, very time consuming. On the other hand, automatic segmentation methods offer faster results, but they require high-quality images with sufficient contrast to achieve accuracy. Most automatic segmentation algorithms rely on intensity values within the image. These algorithms have proven successful in segmenting CT images, where density is directly related to Hounsfield units. However, in MRI, intensity values do not correspond to a definitive physical measurement. Different tissues can exhibit similar intensity values, making segmentation more complex in MRI. The algorithms are not able to distinguish between the dark intensities in the vertebrae body and the dark intensity in the anterior part of the cervical spine, resulting in the segmentation extending beyond its intended regions. This effect are highlighted in Figures 22 to 28 in Appendix B.

Although ITK-SNAP is an easy to use and accessible software for segmentation, it has some limitations. When performing automatic segmentation methods, a rectangular box is used to delineate the segmentation region. ITK-SNAP do not provide flexibility in manipulating the segmentation box. Users can only define the size and placement of the box, as it does not allow for tilting at an angle or accommodating curved shapes. By placing the segmentation box with greater precision, the issue of segmenting poorly contrasted regions could potentially be overcome. The size, shape and placement of the subjects' cervical spine differed. The cervical spine of the last three subject was more or less in line with the z-direction of the magnet, accommodating the placement of the segmentation box, see Appendix B. This is reflected in the DSC values in table 1. The cervical spine of the first subject exhibited an angle with respect to the z-direction, while the second subject had a curved cervical spine.

A significant challenge in UHF MRI arises from the inhomogeneity in the transmit and receive fields, which cause image intensity shading and variable tissue contrast within an image. Improving image quality in UHF MRI of the spinal cord necessitates research and development in coil design. In this thesis, the RF coil was approved for both research purposes in late February of 2023. Among the initial images captured using this coil, subjects participating in this study were included. However, inadequate transmit voltage during the imaging of the initial subjects (not included in this study) resulted in reduced signal in the imaging volume. Due to the poor signal, these subjects were not included in the study. Even after appropriate adjustment of the transmit voltage, the contrast in the anterior part of the cervical spine remained poor for all subjects. The difference in contrast between the anterior and the posterior part of the cervical spine can clearly be seen in the MR images in Figure 17 and Figures 22 to 28. The same figures highlights the difficulties the semi-automatic and automatic segmentation methods had in distinguishing the cervical spine from adjacent soft tissue, especially in the anterior part of the cervical spine. The effect can be seen in the semi-automatic and automatic segmentations of every subject.

This outcome can be primarily attributed to the sub-optimal design of the surface coil, which gives an inhomogeneous transmit and receive $B_1$ field . By achieving better contrast in the anterior part of the spine, the automatic and semi-automatic segmentations could yield more successful and useful results.

The segmentations were assigned a uniform susceptibility distribution and used to simulate the induced magnetic field distortions. Initially, the simulated $B_0$ field distortions were performed with segmentations obtained from the MP2RAGE sequence. However, since the field map sequence and the MP2RAGE sequence are from different measurements, there were possibilities that the subject had moved. A small movement would greatly influence the fit between the simulated and measured field maps. To address this, manual segmentations of the cervical spine were performed on the magnitude image from the field map sequence for each subject, enabling a direct slice-to-slice and voxel-to-voxel comparison. Even tough, the segmentation from the high resolution MP2RAGE images were not used in this thesis to simulate the induced magnetic field distortions, they have great future utility. High resolution segmentations would provide high resolution simulations with the potential of optimizing the MR sequence and shimming techniques.

The segmentations were assigned a susceptibility value of 0.19 ppm, reflecting the difference in the susceptibility value between bone and water, as described by Schenck [14]. However, the linear fit points to a mean difference in susceptibility value of approximately -1.28 ppm. The susceptibility value of soft tissue are close to that of water at -9 ppm, meaning that bone in fact are more diamagnetic than soft tissue. After a renewed literature search, several sources work with a difference in susceptibility between bone and soft tissue of -2.1 ppm $\pm$ 0.6, [28, 29], thus supporting the findings in this thesis.

The linear regression analysis performed on the measured and simulated field maps are the basis of the result. All MR scans are subject to hardware related noise or noise from thermal motion. To mitigate the noise, the field maps were acquired with thick slices of 2.4 mm and a large FOV. However, some noise will be present and possibly affecting the values in the measured field map and thus the linear fit. The measured field maps are from the neck region of healthy subjects, meaning they consisting of several other tissue types, and not only the cervical spine. Inhomogeneities in the background field, not caused by the cervical spine may also affect the fit of the regression analysis. The remarkable resemblance between the field maps, most notably in Figure 20 and 32 are due to the susceptibility distribution in the cervical spine, but t is important to state that the other two factors may have influenced the linear fit.

The gradient in the z-axis calculated in the measured field maps suffer from extensive noise. Dipole effects can be seen around the spinal process, but the pattern in the spinal canal of the simulated field is not visible in the measured gradient map. Smoothing of these field should provide better visibility, as done by A. Schmidt [27], but time limitations prevented this procedure.

Lastly, optimization of the MR sequence of the field map can provide high resolution field maps to compare against the high resolution simulations. By altering the acquisition parameters, enhanced contrast between bone and adjacent soft tissue can be obtained, facilitating improved segmentation.

# 6 Future Work

The work conducted in this thesis demonstrates the potential of calculating patient-specific field inhomogeneity maps through direct segmentation of MR images. However, the best results were achieved with manual segmentations, which require significant time investment. To address the issue of time consumption, semi-automatic segmentation and automatic segmentation methods were tested. These methods showed promising results, but also had challenges in distinguishing the cervical spine from the adjacent soft tissue, especially in the anterior part of the cervical spine. Better contrast in these regions could facilitate the use of (semi-)automatic segmentations. To achieve this, a revision and optimization of the MR sequence deployed are necessary.

Another area that holds great promise is the application of artificial intelligence (AI) or deep learning algorithms for segmentation purposes. In pursuit of suitable segmentation software, efforts were made to collaborate with two AI developers specializing in medical image segmentation. Unfortunately, the collaboration did not materialize due to insufficient data.

# 7 Conclusion

In this master thesis, segmentation of the cervical spine were used to simulate induced magnetic field distortions and compare it to measured field distortions from the MR scanner.

Manual segmentations of the cervical spine from high resolution MP2RAGE images were successfully obtained from five healthy subjects, and used as the gold standard against which (semi-)automatic segmentations were compared. Although the latter methods showed potential, they encountered challenges in accurately segmenting poorly contrasted region, especially the anterior part of the cervical spine.

In the second part, simulations of induced magnetic field distortions from the susceptibility distribution in the cervical spine were compared to the measured field distortions at the scanner. Through linear regression analysis, a remarkable resemblance was shown between the simulated and measured frequency maps, indicating that the field distortions in the spinal canal are mainly caused by the changing susceptibility value between the cervical spine and the adjacent soft tissue. The results from linear fit indicates that the difference in susceptibility between bone and soft tissue is approximately -1.28 ppm.

The work in this master's thesis can contribute to increased knowledge about segmentation of bones from MRI, and how the susceptibility distribution in the cervical spine creates distortions in the $B_0$ magnetic field, affecting image quality in MRI of the spinal cord. The results can facilitate optimization of shimming techniques and MR sequences to enhance MRI of the spinal cord.

# Bibliography


[1] Sebastian A. D. Sandbu. 'Modeling Susceptibility-Induced Magnetic Field Distributions from the Neck and Spinal Cord'. In: (2022).

[2] Alessio Virzì et al. 'Comprehensive review of 3D segmentation software tools for MRI usable for pelvic surgery planning'. In: *Journal of digital imaging* 33.1 (2020), pp. 99–110.

[3] R. Salomir, B. D. de Senneville and C. TW. Moonen. 'A fast calculation method for magnetic field inhomogeneity due to an arbitrary distribution of bulk susceptibility'. In: *Concepts in Magnetic Resonance Part B: Magnetic Resonance Engineering* (2003). URL: https://onlinelibrary.wiley.com/doi/abs/10.1002/cmr.b.10083.

[4] J.P. Marques and R. Bowtell. 'Application of a Fourier-based method for rapid calculation of field inhomogeneity due to spatial variation of magnetic susceptibility'. In: *Concepts in Magnetic Resonance Part B: Magnetic Resonance Engineering* (2005). URL: https://onlinelibrary.wiley.com/doi/abs/10.1002/cmr.b.20034.

[5] Robert W. Brown et al. *Magnetic Resonance Imaging: Physical Principles and Sequence Design*. Wiley Blackwell, 2013.

[6] Z. P. Liang and P. C. Lauterbur. *Principles of Magnetic Resonance Imaging: A Signal processing Persepctive*. Wiley-IEEE Press, 1999.

[7] Pierre-Marie Robitaille and Lawrence J. Berliner. *Ultra High Field Magnetic Resonance Imaging*. Springer, 2006.

[8] Michael Markl and Jochen Leupold. 'Gradient echo imaging'. In: *Journal of Magnetic Resonance Imaging* 35.6 (2012), pp. 1274–1289. DOI: https://doi.org/10.1002/jmri.23638. eprint: https://onlinelibrary.wiley.com/doi/pdf/10.1002/jmri.23638. URL: https://onlinelibrary.wiley.com/doi/abs/10.1002/jmri.23638.

[9] Andrew Murphy and Frank Gaillard. 'MRI sequences (overview)'. In: *Radiopaedia.org*. Radiopaedia.org, June 2015.

[10] Thomas Puiseux et al. 'Numerical simulation of time-resolved 3D phase-contrast magnetic resonance imaging'. In: *PLOS ONE* 16 (Mar. 2021), e0248816. DOI: 10.1371/journal.pone.0248816.

[11] J P Mugler 3rd and J R Brookeman. 'Rapid three-dimensional T1-weighted MR imaging with the MP-RAGE sequence'. en. In: *J. Magn. Reson. Imaging* 1.5 (Sept. 1991), pp. 561–567.

[12] Mathieu Boudreau. *MP2RAGE: T1 mapping*. en. 2019. URL: https://qmrlab.org/2019/04/08/T1-mapping-mp2rage.html.

[13] Mark Tanner et al. 'Fluid and white matter suppression with the MP2RAGE sequence'. en. In: *J. Magn. Reson. Imaging* 35.5 (May 2012), pp. 1063–1070.

[14] J. F. Schenck. 'The role of magnetic susceptibility in magnetic resonance imaging: MRI magnetic compatibility of the first and second kinds'. In: *Med Phys.* (1996).

[15] Qing X. Yang, Michael B. Smith and Jianli Wang. 'Magnetic Susceptibility Effects in High Field MRI'. In: *Ultra High Field Magnetic Resonance Imaging*. Springer US, 2006. URL: https://doi.org/10.1007/978-0-387-49648-1_9.

[16] Emine U. Saritas, Samantha J. Holdsworth and Roland Bammer. 'Chapter 2.3 - Susceptibility Artifacts'. In: *Quantitative MRI of the Spinal Cord*. Ed. by Julien Cohen-Adad and Claudia A.M. Wheeler-Kingshott. San Diego: Academic Press, 2014, pp. 91–105. ISBN: 978-0-12-396973-6. DOI: https://doi.org/10.1016/B978-0-12-396973-6.00007-1. URL: https://www.sciencedirect.com/science/article/pii/B9780123969736000071.

[17] Kevin M Koch, Douglas L Rothman and Robin A de Graaf. 'Optimization of static magnetic field homogeneity in the human and animal brain in vivo'. en. In: *Prog. Nucl. Magn. Reson. Spectrosc.* 54.2 (Feb. 2009), pp. 69–96.

[18] K. Wachowicz. 'Evaluation of active and passive shimming in magnetic resonance imaging'. In: *Research and Reports in Nuclear Medicine* (2014).

[19] Mathias Blasche, Daniel Fischer and Siemens Healthineers. 'Magnet homogeneity and shimming'. In: *Siemens Healthineers*. Siemens Healthcare GmbH Erlangen, Germany, White Paper, 2017.

[20] Robert L Barry et al. 'Spinal cord MRI at 7T'. In: *Neuroimage* 168 (2018), pp. 437–451.

[21] Ivana Despotović, Bart Goossens and Wilfried Philips. 'MRI segmentation of the human brain: challenges, methods, and applications'. In: *Computational and mathematical methods in medicine* 2015 (2015).

[22] Dinesh D Patil and Sonal G Deore. 'Medical image segmentation: a review'. In: *International Journal of Computer Science and Mobile Computing* 2.1 (2013), pp. 22–27.

[23] A. Schäfer et al. 'Using magnetic field simulation to study susceptibility-related phase contrast in gradient echo MRI'. In: *NeuroImage* (2009). URL: https://www.sciencedirect.com/science/article/pii/S1053811909006065.

[24] Antal Nógrádi and Gerta Vrbová. 'Anatomy and Physiology of the Spinal Cord'. In: *Transplantation of Neural Tissue into the Spinal Cord*. Boston, MA: Springer US, 2006, pp. 1–23. ISBN: 978-0-387-32633-7. DOI: 10.1007/0-387-32633-2_1. URL: https://doi.org/10.1007/0-387-32633-2_1.

[25] Xiangrui Li et al. 'The first step for neuroimaging data analysis: DICOM to NIfTI conversion'. en. In: *J. Neurosci. Methods* 264 (May 2016), pp. 47–56.

[26] Paul A. Yushkevich et al. 'User-Guided 3D Active Contour Segmentation of Anatomical Structures: Significantly Improved Efficiency and Reliability'. In: *Neuroimage* 31.3 (2006), pp. 1116–1128.

[27] Annelen D. Scmidt. *Modeling Susceptibility-induced Magnetic Field Distortion in the Human Head at 7 Tesla Using a Fourier-based Method*. 2022.

[28] Jeffrey A. Hopkins and Felix W. Wehrli. 'Magnetic susceptibility measurement of insoluble solids by NMR: Magnetic susceptibility of bone.' In: *Magnetic Resonance in Medicine* 37.4 (Apr. 1997), pp. 494–500. DOI: 10.1002/mrm.1910370404. URL: https://doi.org/10.1002/mrm.1910370404.

[29] Sagar Buch et al. 'Susceptibility mapping of air, bone, and calcium in the head'. In: *Magnetic Resonance in Medicine* 73.6 (2015), pp. 2185–2194. DOI: https://doi.org/10.1002/mrm.25350. eprint: https://onlinelibrary.wiley.com/doi/pdf/10.1002/mrm.25350. URL: https://onlinelibrary.wiley.com/doi/abs/10.1002/mrm.25350.

# Appendix

## A Matlab functions

```
%Fourier transformations, k-space:
function [B_kspace] = SusMap_Kspace(Obj,dr)
%Input units:
%[obj] = unitless / susceptibility map
%[dr] = mm
[M, N, L] = size(Obj);

Obj_tilde = fftshift(fftn(Obj));
% fftn returns the Fourier transformasjonen til Obj. fftshift shifts
% zero-frequency components to the centre of the spectrum.
%Obj_tilde = tall(Obj_tilde);
clear Obj

[Dipole_map] = dipole(M,N,L,dr);
clear M N L dr

B_kspace = Obj_tilde.*Dipole_map; %Unit: dimensionless. Equal to B_z(k)/B_0. Objektet multiplied b


end

function [SusImageSpace] = ImageSpace_SusMap(B_kspace)
% Output: Image domain representation of B_kspace
SusImageSpace = ifftn(ifftshift(B_kspace));

end

function [Dipole]= dipole(M,N,L,dr)
%Input units:
%[dr] = mm
%Output: Dipole field defined in k-space

dy = dr(1)*10^(-3); %units: m
dx = dr(2)*10^(-3);
dz = dr(3)*10^(-3);

dky = cast((2*pi/(M*dy)),'single'); %units: rad/m
dkx = cast((2*pi/(N*dx)),'single');
dkz = cast((2*pi/(L*dz)),'single');

%clear dy dy dz dr
```

```
ky = ((-M/2)*dky:dky:(M/2-1)*dky);
kx = ((-N/2)*dkx:dkx:(N/2-1)*dkx);
kz = ((-L/2)*dkz:dkz:(L/2-1)*dkz);

clear dky dkx dkz M N L

[kx,ky,kz] = meshgrid(kx,ky,kz);

Dipole = 1/3-(kz.^(2))./(kx.^2 + ky.^2 + kz.^2); %units: unitless
clear kx ky kz krho
Dipole(isnan(Dipole)) = 0;

end
```

# B Segmentations

In this section, the segmentations from subject 1, 3, 4 and 5 are presented. They are presented in a similar fashion as for the second subject, comparing the (semi-)automatic segmentation with the manual segmentation. Each subject have their own subsection, providing a clear overview of the segmentations.

The highest DSC values were from subject 3, 4 and 5. Each with the alignment of their spine parallel to the direction of the $B_0$ field. This can be seen in the Figures 24, 26 and 28.

### B.1 First Subject

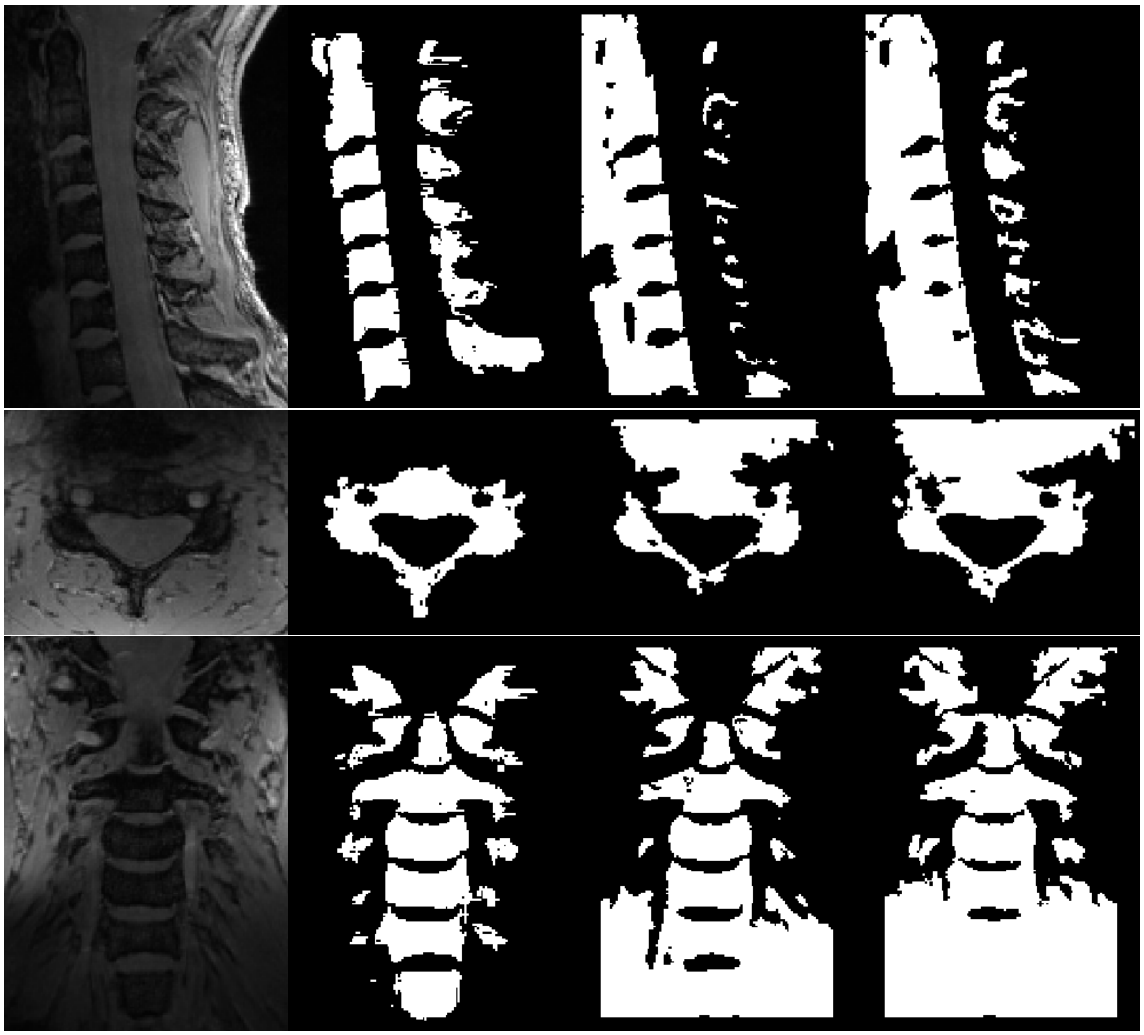

Figure 22: Comparison of the segmentations from the first subject. From left to right: a) MRI, b) manual segmentation, c) semi-automatic segmentation, and d) automatic segmentation. Top to bottom, the sagittal plane, the transverse plane and the coronal plane.

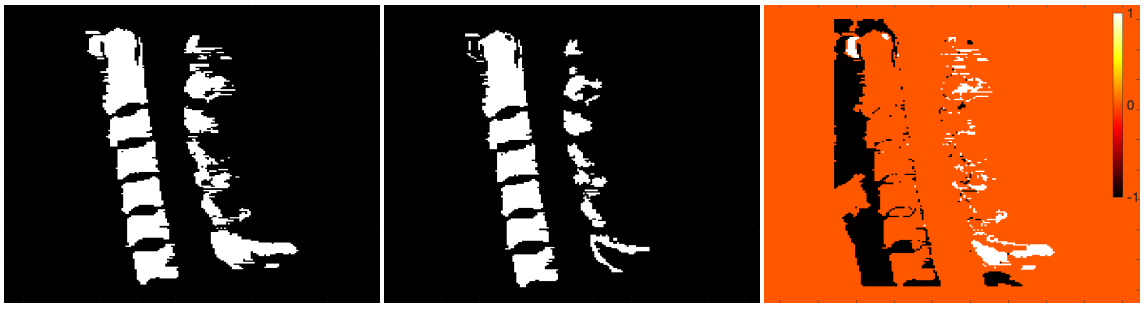


Figure 23: Visualisation of how the automatic segmentation method performs compared to the manual segmentation for the first subject. From left to right, a) the manual segmentation, b) matrix containing similarities, "true positives", and c) the difference, "false positives" in black and "false negatives" in white.

### B.2 Third subject

Figure 24: Comparison of the segmentations from the third subject. From left to right: a) MRI, b) manual segmentation, c) semi-automatic segmentation, and d) automatic segmentation. Top to bottom, the sagittal plane, the transverse plane and the coronal plane.

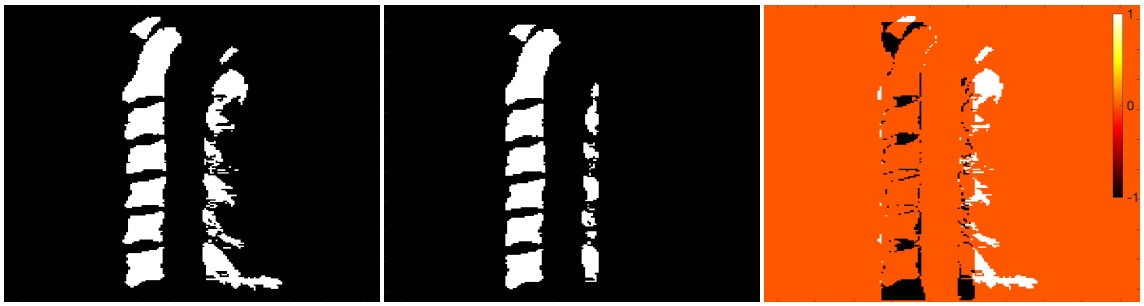


Figure 25: Visualisation of how the semi-automatic segmentation method performs compared to the manual segmentation for the third subject. From left to right, a) the manual segmentation, b) matrix containing similarities, "true positives", and c) the difference, "false positives" in black and "false negatives" in white

### B.3 Fourth Subject

Figure 26: Comparison of the segmentations from the fourth subject. From left to right: a) MRI, b) manual segmentation, c) semi-automatic segmentation, and d) automatic segmentation. Top to bottom, the sagittal plane, the transverse plane and the coronal plane.


Figure 27: Visualisation of how the semi-automatic segmentation method performs compared to the manual segmentation for the fourth subject. From left to right, a) the manual segmentation, b) matrix containing similarities, "true positives", and c) the difference, "false positives" in black and "false negatives" in white

### B.4 Fifth Subject

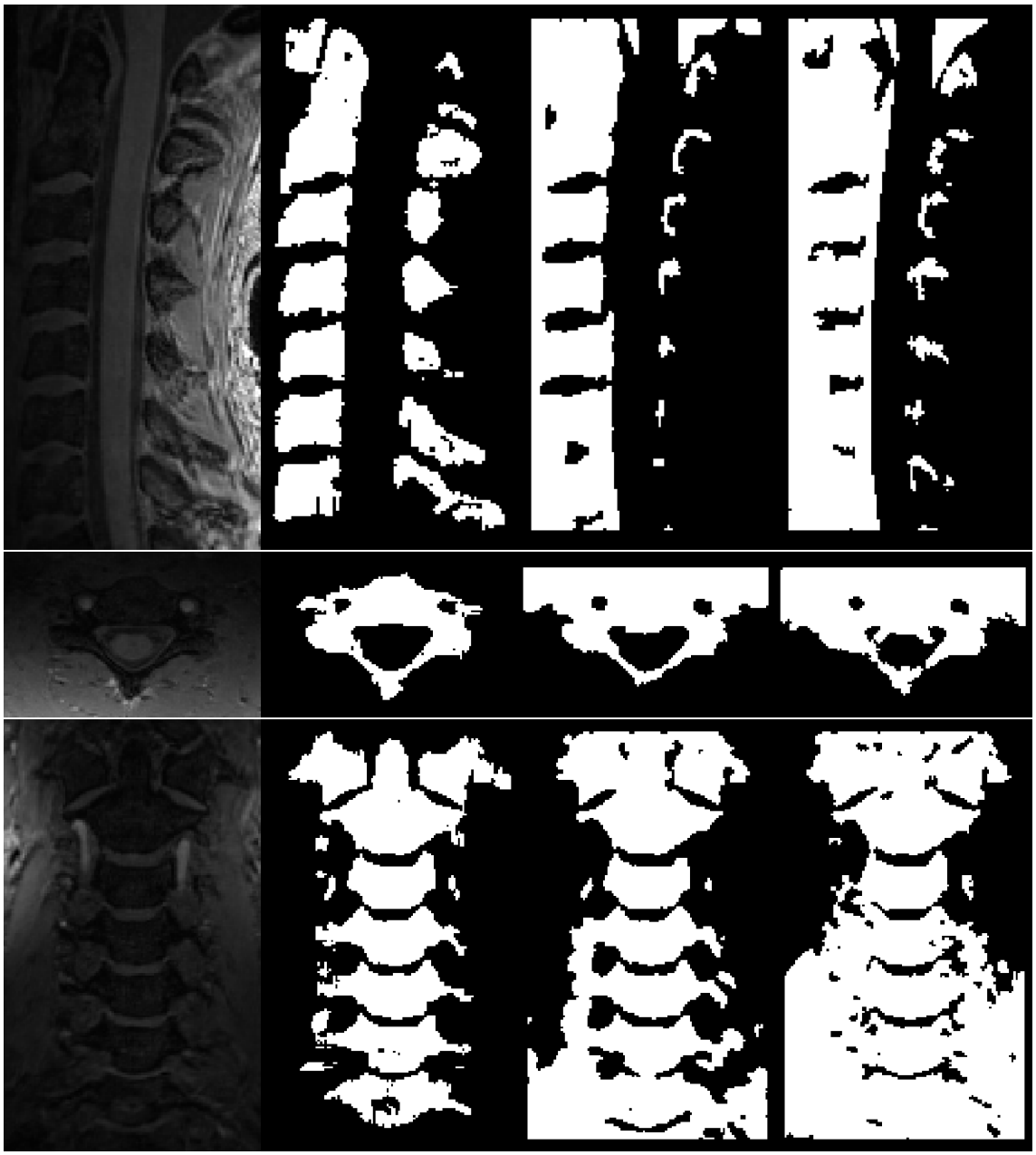

Figure 28: Comparison of the segmentations from the fifth subject. From left to right: a) MRI, b) manual segmentation, c) semi-automatic segmentation, and d) automatic segmentation. Top to bottom, the sagittal plane, the transverse plane and the coronal plane.


Figure 29: Visualisation of how the automatic segmentation method performs compared to the manual segmentation for the fifth subject. From left to right, a) the manual segmentation, b) matrix containing similarities, "true positives", and c) the difference, "false positives" in black and "false negatives" in white

## C Frequency Offset and Gradient Maps

The frequency field maps and gradient in the z-direction for the first, third and fifth subject are presented in this section. Phase images of the fourth subject were not acquired during the scanning.

The frequency maps of first subject differ the most from the rest. This is expressed in terms of the large offset of -210.87, calculated from the linear regression in table 2. Due to this offset, the limit in the intensity values of the image were set to [0, 300], as shown in the color bar in Figure 30.

### C.1 First Subject

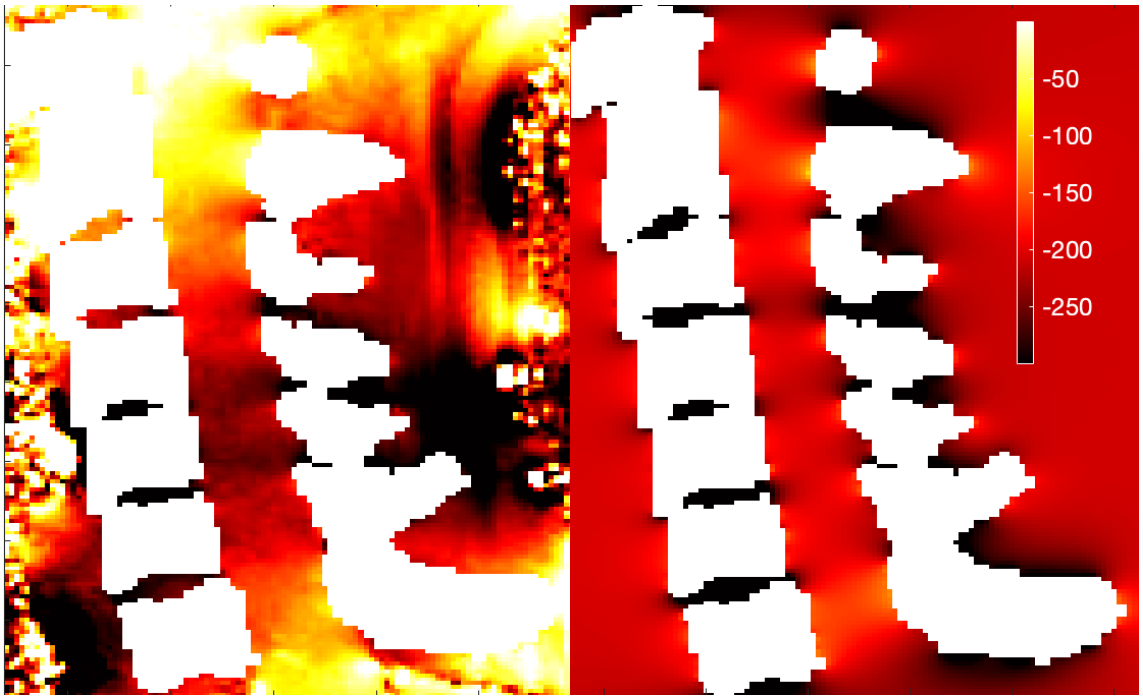


Figure 30: Measured field map to the left and simulated field map to the right.

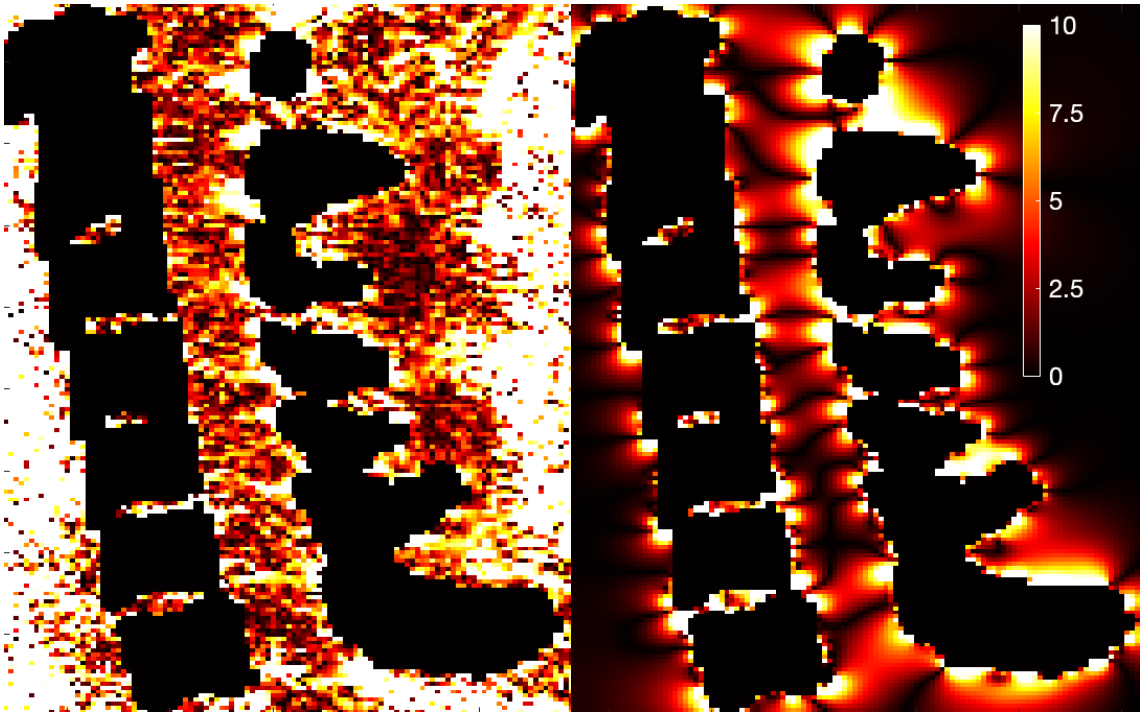


Figure 31: Calculated gradient frequency offset in z-direction.

## C.2 Third Subject

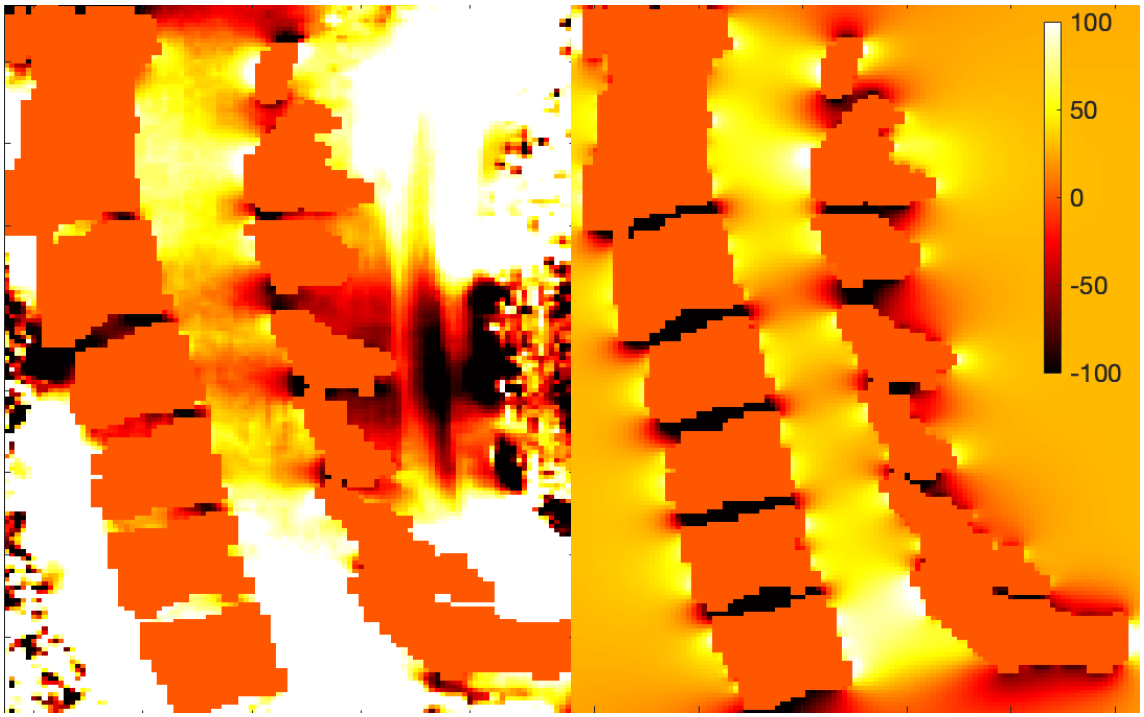


Figure 32: Measured field map to the left and simulated field map to the right.

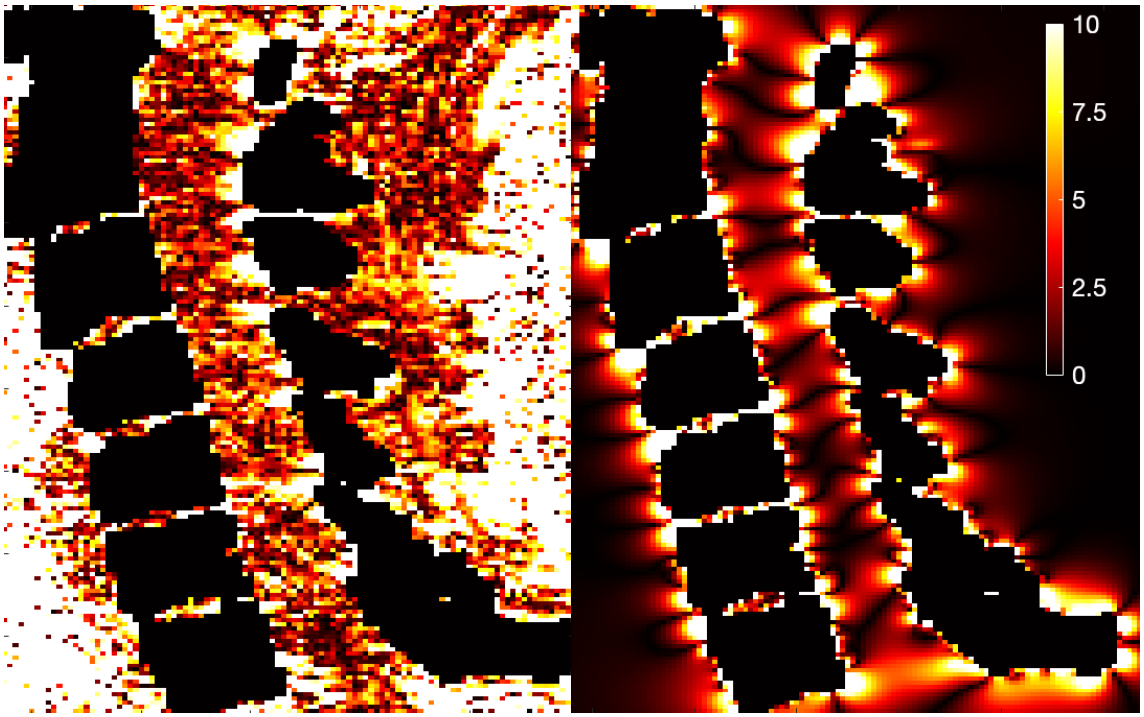


Figure 33: Calculated gradient frequency offset in z-direction.

### C.3 Fifth Subject

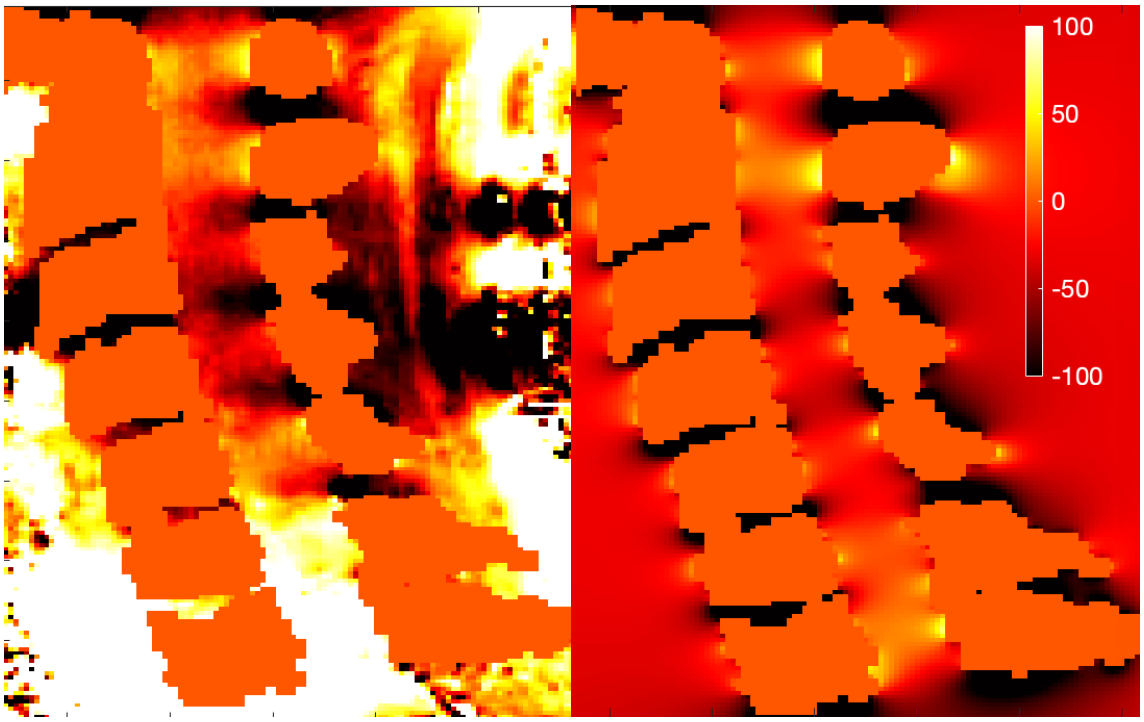


Figure 34: Measured field map to the left and simulated field map to the right.

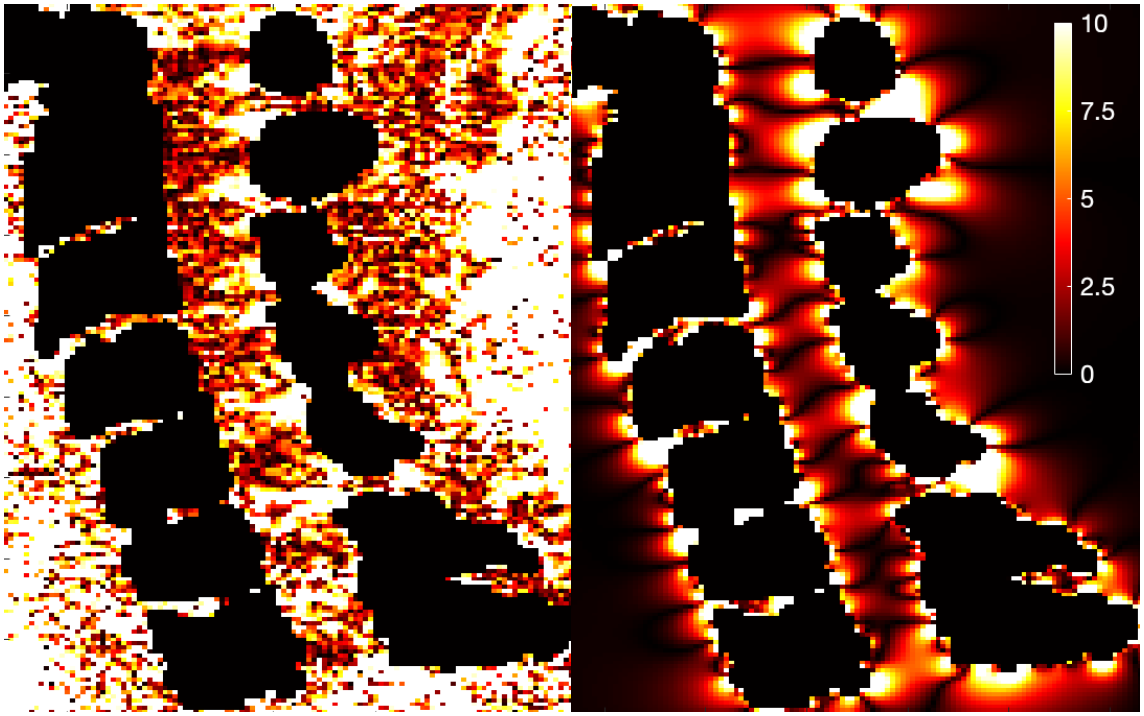


Figure 35: Calculated gradient frequency offset in z-direction.

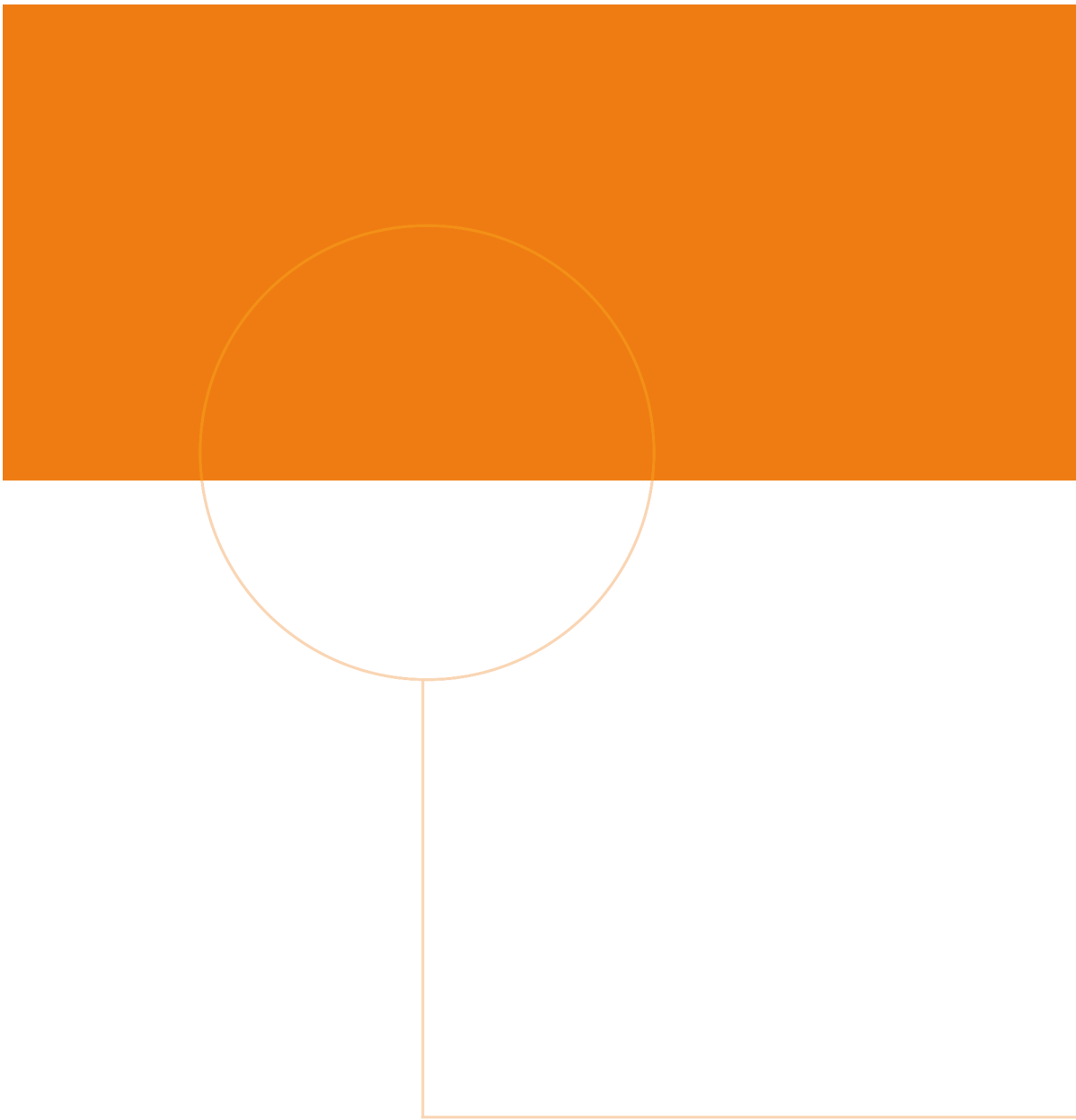

NTNU

Norwegian University of
Science and Technology